

FUNDAMENTAL RESONANT FREQUENCIES DERIVED FROM SHALLOW
SEDIMENT PROPERTIES FOR THE CHARLESTON, SOUTH CAROLINA AREA

by

William Dale Schermerhorn



A thesis

submitted in partial fulfillment

of the requirements for the degree of

Master of Science in Geophysics

Boise State University

August 2021

© 2021

William Dale Schermerhorn

ALL RIGHTS RESERVED

BOISE STATE UNIVERSITY GRADUATE COLLEGE

DEFENSE COMMITTEE AND FINAL READING APPROVALS

of the thesis submitted by

William Dale Schermerhorn

Thesis Title: Fundamental Resonant Frequencies Derived From Shallow Sediment Properties for the Charleston, South Carolina Area

Date of Final Oral Examination: 23 April 2021

The following individuals read and discussed the thesis submitted by student William Dale Schermerhorn, and they evaluated his presentation and response to questions during the final oral examination. They found that the student passed the final oral examination.

Lee M. Liberty, M.S. Chair, Supervisory Committee

Dylan Mikesell, Ph.D. Member, Supervisory Committee

Brittany Brand, Ph.D. Member, Supervisory Committee

The final reading approval of the thesis was granted by Lee M. Liberty, Chair of the Supervisory Committee. The thesis was approved by the Graduate College.

DEDICATION

I dedicate this thesis to the memory of my late father, Alan Michael Schermerhorn (1943-2018). You were always a beacon of support and guidance in my life. May you rest peacefully.

ACKNOWLEDGEMENTS

First and foremost, I would like to give special thanks to my thesis advisor, Lee Liberty, who taught me to be a better scientist. Lee has taught me to approach scientific problems from all angles, leaving no stone unturned, and has opened my eyes to the wide variety of scientific problems that the field of seismology can be used study.

Secondly, I would like to acknowledge my committee members Dr. Brittany Brand and Dr. Dylan Mikesell for their insightful advice, questions, and support. I would like to thank Thomas Pratt of the USGS, whom collaborated with Lee and I on this work, offering thoughtful feedback and useful discussion. I would like to thank Thomas Otheim and Thomas harper for collection of this dataset, prior to my time at Boise State University.

Lastly, I would like to thank my family and friends. First and foremost, I would like to thank my mother, Karen Schermerhorn, and sister, Jonelle Schermerhorn for their endless support and encouragement. I would like to thank my partner and our dog for keeping me well grounded. There are also a number of friends from ERB and elsewhere who have always offered good perspective, feedback, and made my time in graduate school a ton of fun.

ABSTRACT

Large historic earthquakes, low velocity near surface sediments, a poor understanding of earthquake sources, and a growing population base for the Charleston, South Carolina area suggest robust site response and active fault maps are needed. A Boise State University team acquired 14 km of new surface-based seismic data to obtain surface wave dispersion curves and reflection images for the southern isoseismal region of the 1886 earthquake. From these data, I generate shear wave velocity (V_s)-depth profiles through a grid search approach. I integrate my results with other published data to develop a soil thickness and high frequency fundamental resonance maps for the Charleston region. From the reflection data, I identify faults that may be Quaternary active, as they are co-located with surface deformation features observed in 1886. The Boise State University rapid seismic land streamer acquisition system produces robust dispersion and reflection data that may be applicable for other areas within the Atlantic Coastal Plain, where shallow high impedance boundaries and faults that offset Tertiary strata are common.

TABLE OF CONTENTS

DEDICATION	iv
ACKNOWLEDGEMENTS	v
ABSTRACT	vi
LIST OF TABLES	ix
LIST OF FIGURES	x
LIST OF ABBREVIATIONS	xiv
CHAPTER ONE: INTRODUCTION	1
Geologic and Tectonic Setting.....	4
Seismic Properties.....	8
CHAPTER TWO: DATA AND METHODOLOGY	10
Data	10
Vs Derived from Surface Waves – Grid Search Approach.....	11
Sensitivity Analysis.....	15
Reflection Profiling.....	16
CHAPTER THREE: GRID SEARCH AND REFLECTION PROFILING RESULTS ...	18
Railroad Avenue Seismic Profile.....	18
Martin Street and CSX Seismic Profiles	20
Hughes Road Seismic Profile	23
CHAPTER FOUR: DISCUSSION.....	26

Vs Comparisons to Lithology	26
High frequency Fn Derived from Soil Thickness and Vs.....	30
Constructing a Regional Site Response Parameter Database for the Greater Charleston Region	32
Spatial Variability in Vs, Quaternary Thickness, and Fn	40
Liquefaction and Ground Deformation Potential.....	43
MASW and SCPT differences	44
Fault Interpretations.....	46
CHAPTER FIVE: CONCLUSIONS	49
REFERENCES	50

LIST OF TABLES

Table 1.1	Unsaturated and saturated grid search model parameters. V_p (upper and lower layer) and lower layer V_s units are m/s, V_{s1} unit is a percent scalar of the Rayleigh-wave phase velocity, density (ρ) units are kg/m ³ , and depth unit is meters.....	13
Table 1.2	Saturated 2-layer Grid Search Model Statistics.	27
Table 1.3	CPT Statistics (Andrus et al. 2016).....	27

LIST OF FIGURES

- Figure 1. (a) Topographic map with seismic profile and Woodstock fault location (Talwani and Dura-Gomez, 2009) within the southern 1886 isoseismal region. Seismic profiles with fault locations (X and yellow circles) are Martin, CSX, Railroad, and Hughes 1 and 2 (black lines) and legacy seismic data (blue lines) are from Marple and Miller (2006). Also shown are surface deformation features (Dutton, 1889), boreholes (Weems et al. 2014), and Woodstock and Rantowles 1886 epicenter locations (Marple & Hurd 2020). The inset map shows the complete isoseismal region (Dutton in 1889) and earthquake epicenters. AR=Ashley River, SR=Stono River, CR=Cooper River, WR=Wando River (WR), MPSSZ=Middleton Place-Summerville Seismic Zone, S=Summerville. (b) Simplified surficial geologic map, modified from Weems et al. (2014) overlain on topography. 3
- Figure 2. Fault interpretation for the greater Charleston region with earthquake epicentral locations: (a) Marple and Miller (2006) model of the Woodstock Fault (WF) as a continuous fault with a 12° fault bend; (b) Talwani and Dura-Gomez (2009) Woodstock fault stepover model; (c) Weems et al. (2014) Woodstock fault stepover model. S= Summerville; Char= Charleston. Yellow stars represent 1886 Woodstock and Rantowles epicenter locations (Marple and Hurd, 2020). Woodstock fault (WF), where N and S define the northern and southern fault strands in (b) and (c). SF=Summerville fault; ARF=Ashley River fault; SBF=Sawmill Branch fault; LF=Lincolnvilleville fault; CF=Charleston fault; ADRF=Adams Run fault; BF=Berkeley fault. Earthquake locations from 1972 to present are from the U.S. Geological Survey (USGS) comprehensive earthquake catalog (U.S. Geological Survey, 2020)..... 7
- Figure 3. CPT-derived Vs (m/s) - depth (m) profiles with mean values for (a) Man-made fills, (b) Holocene and late Pleistocene deposits, (c) Wando Formation, (d) Ten Mile Hill beds, (e) Penholoway Formation and Daniel Island beds, and (f) Tertiary deposits (modified from Andrus et al. 2006 and Chapman et al. 2006). Quaternary strata (blue) and Tertiary strata (tan). 9
- Figure 4. (a) Unprocessed field record 8420 from Railroad Ave showing low-velocity surface waves that dominate the wavefield. (b) Filtered (30–200 Hz) field record of (a), confirming soil saturation from 1500 m/s first-arrival wave speed. (c) Dispersion image from (a). I pick the fundamental

mode of the Rayleigh wave (indicated by yellow points on panel (c)).
 Figure 5 revised from Liberty et al. (2021).....11

- Figure 5. (a) Fundamental mode dispersion curves for two-layer over half-space models. These models represent 5, 15, and 25 m of Quaternary sediments over Tertiary sedimentary bedrock. Velocities and densities are in m/s and g/cc units, respectively. Dashed lines represent dry soil over bedrock models, whereas solid lines represent saturated soils over bedrock models. (b) RMS error distribution for all upper layer Vs-layer thickness models. (c) RMS error distribution for all lower layer Vs-upper layer thickness models. The black cross on (b) and (c) denotes the global minimum solution.14
- Figure 6. Vs-depth profiles near borehole RA-16. Saturated (blue line) and unsaturated (red line) best-fit two-layer models, 10-layer deterministic Surfseis model (black line), and depth to Tertiary at RA-16 (black dashed line). Best fit, two-layer saturated model solutions using +/- 10 m/s dispersion picks (blue dotted lines) and +/- one standard deviation from the mean value of Tertiary (gray rectangle) are from Andrus et al. (2006).16
- Figure 7. Two-layer best fit model for the one-km long Railroad profile. Horizontal axis is in shot gathers with consecutive shot gathers spaced 2.5 m apart. (a) Picked dispersion frequency range (black lines), with the estimated cutoff frequency of Xia et al. 1999 (purple points). (b) Quaternary (Vs1) and Tertiary (Vs2) layer Vs velocities. (c) Model misfit (difference between observed and calculated). (d) 2-layer shear wave velocity model from 433 1-D best fit models. Green line indicates water table elevation from refraction analysis. The black vertical line indicates the location and depth to Tertiary strata encountered in borehole RA-16. Horizontal black lines indicate the resulting depth to Tertiary for phase velocity perturbation of +/- 10 m/s applied to dispersion picks. Black rectangle (top right) indicates the length of the geophone array. (e) Resonant frequency yellow and impedance (blue) along the transect. (f) Reflection cross section from this transect in the upper 500 meters. The location of lateral displacements mapped by Dutton in 1889 (red crosses).19
- Figure 8. (a) Vs1 and Vs2 best fit solutions for Martin and CSX profiles. Horizontal axis is in shot gathers with consecutive shot gathers spaced 2.5 m apart. (b) 2-layer best fit Vs models for Martin and CSX profiles. The location of lateral displacements mapped by Dutton in 1889 (red crosses), land streamer length, and borehole constraints (black vertical lines) are shown. (c) Composite reflection cross section with ~8:1 vertical exaggeration for Martin and CSX in two-way travel time(s). Interpreted faults on (c) are indicated by black lines.22

Figure 9.	(a) Vs1 and Vs2 best fit solutions for Hughes 1 and 2. Horizontal axis is in shot gathers with consecutive shot gathers spaced 2.5 m apart. (b) 2-layer Grid Search Vs models for Hughes 1 and 2. Borehole constraints for depth to top of Tertiary strata from RA-20 is shown (b). (c) Composite reflection images with ~3:1 vertical exaggeration in estimated depth. Interpreted faults on (c) are indicated by black lines..... 25
Figure 10.	Vs-depth plots for three lithologies. Andrus et al. (2006) CPT data (black circles), MASW Vs best fit models for fully saturated (blue circles), and unsaturated (red circles). Black line and Vs value labeled on plots indicates median Vs values from CPT data. (a) Holocene-Late Pleistocene (units Qhm, Qht, & Qsbc), (b) Bulk Wando Formation (units Qwc and Qwls), (c) Bulk Ten Mile Hill Beds (units Qtc and Qts). (d) relative density histogram for Vs for all Quaternary units from this study with a theoretical normal distribution overlain (red line). The mean and standard deviation are shown. 29
Figure 11.	(a) Fn histogram by bulk lithology and (b) Fn - Quaternary thickness cross plot color coded by bulk lithology. A power law function fit to the BSU data is (solid black line) from equation 2 and constant velocity of 200 m/s -Fn relationship (dashed line) used by Chapman et al. (2006). 31
Figure 12.	Greater Charleston region topographic map showing BSU seismic transects (purple lines), auger holes (Weems et al., 2014) (red circles), and SCPT sites from Gathro (2018) (black triangles). Major cities (yellow circles) and major rivers and waterways are labeled. A=Ashley River, C=Cooper River, W=Wando River, S=Stono River, E=Edisto River, CS=Cypress Swamp..... 32
Figure 13.	Vs (m/s)-depth (m) plots of weighted running average SCPT data (black), plus one standard deviation (red), and minus one standard deviation (blue) for 11 individual lithologies from Gathro (2018). The magenta line is the linear least squares fit to each running average dataset, and the equation for this line is shown in the top left corner of each plot..... 34
Figure 14.	Vs-Quaternary thickness for all measurements from the greater Charleston region. The weighted running average of SCPT measurements from Gathro (2018) is indicated by triangles, individual SCPT sites are indicated by circles, and the 2-layer 2D grid search results are indicated by squares. Data points are colored by respective geologic formation. The solid black line indicates a linear least square fit (equation 3, shown in top left) to the weighted running average SCPT dataset used to estimate Vs as a function of Quaternary thickness for the auger holes..... 36
Figure 15.	(a) Interpolated Quaternary Vs for the greater Charleston region derived from SCPT, BSU, and auger hole datasets. The Woodstock fault (Talwani

and Dura-Gomez, 2009) is shown as a solid black line, the 1886 epicenter locations are indicated by green stars (Marple and Hurd, 2020). R=Rantowles and W=Woodstock. Deformation features mapped by Dutton (1889) include lateral displacements, liquefaction craterlets, and rail-line deformation. (b) Same map as above, but now the 1886 isoseismal map from Dutton (1889) is displayed.....37

Figure 16. Fn-Quaternary thickness plot from SCPT data (black circles) BSU data (blue circles), and the larger circles are Vs derived from auger hole data. The green line shows the BSU power law fit (equation 2), while the red solid line shows the SCPT power law fit (equation 4).39

Figure 17. (a) Quaternary thickness map for the greater Charleston region. The Woodstock fault (Talwani and Dura-Gomez, 2009) is shown as a black line, deformation features mapped by Dutton (1889) include lateral displacements, liquefaction craterlets, and rail-line deformation. Exposed Tertiary rocks are indicated by red polygons. (b) Resonant frequency map for the greater Charleston region. The 1886 epicenter locations (green stars) from Marple & Hurd (2020) and the Dutton (1889) isoseismal zone (black polygon)41

Figure 18. (a) Map of my study area showing deformation features, southern isoseismal zone (Dutton, 1889), BSU seismic profiles (black lines), and the Rantowles 1886 epicenter location (green star) from Marple and Miller. (2020). Faults on CSX and Hughes1 (red circles). Faults on Martin St (blue circles) as well as faults identified on USC-5 legacy seismic profile (blue Xs). The proposed location of the Woodstock Fault from Talwani and Dura-Gomez (2009) is indicated by the dashed black line, and proposed fault locations from Pratt et al. (2016) are indicated by the dashed red lines. (b) Reflection imagery from Hughes 1 and 2 in two-way travel time with 3:1 vertical exaggeration. Faults identified on Hughes 1 are shown in red. (c) USC-5 reflection imagery in two-way travel time from Marple and Miller (2006), the two blue arrows indicate faults that may be connected to the structures we observe on Martin St. (d) CSX (right) and Martin St (left) reflection imagery in two-way travel time with 6:1 vertical exaggeration. Fault interpretations are shown in red for CSX and in blue for Martin Street on (d).....48

LIST OF ABBREVIATIONS

V_s	Shear-wave velocity
ρ	Density
F_n	Fundamental resonant frequency
<i>ACP</i>	Atlantic Coastal Plain
MPSSZ	Middleton Place-Summerville Seismic Zone
CPT	Cone Penetrometer Test
SCPT	Seismic Cone Penetrometer Test

CHAPTER ONE: INTRODUCTION

The 1886 Charleston earthquake was the largest historical earthquake in the eastern United States (Frankel et al., 2002; Bakun and Hopper, 2004). This event resulted in over 100 fatalities, and left nearly every building in the Charleston area damaged or destroyed (Bollinger, 1977). A similar earthquake today would be devastating to the region, with significant loss of life and total economic impact as high as \$20 billion (Wong et al., 2005).

The Charleston region is considered the most seismically active region along the eastern U.S. seaboard (Petersen et al., 2014). Although Cramer and Boyd (2014) classified the Charleston earthquake as $\sim M7$, resulting soil liquefaction, ground displacements, and building damage can fit a range of earthquake magnitudes (Ambraseys and Menu, 1988). Because faults related to the 1886 earthquake did not rupture the ground surface, the faults responsible for this earthquake remain elusive. Numerous studies have speculated on active fault locations and kinematics; however, beyond the 1886 earthquake, no direct evidence for Holocene motion on any of the identified faults has been provided. This uncertainty is largely due to the lack of surface fault expression, insufficient subsurface imagery, and limited seismicity recorded with modern instrumentation. Similarly, site response estimates remain sparse.

Although little is currently known about the slip distribution of faults and the related ground motions from 1886, Dutton (1889) outlined an isoseismal epicentral region that incorporated earthquake damage and felt reports (Figure 1). Dutton identified

an initial epicenter near the town of Woodstock, and secondary motion about 20 km to the south near Rantowles. While modern seismicity continues near Woodstock, few earthquakes have been instrumentally recorded within the southern isoseismal zone. High resolution fault mapping and constraints on soil properties will improve our understanding of the earthquake slip history and site response and liquefaction potential.

In this thesis, I focus on the seismotectonics and site response potential of the southern isoseismal area near Rantowles. I present results from five land streamer seismic profiles where I map Cenozoic structure and stratigraphy. I assess local site conditions from shallow p-wave (V_p) and s-wave velocity (V_s) measurements, and compare soil effects observed in 1886 to my estimated soil properties and fault locations. Finally, I integrate my findings with regional studies to develop thickness, V_s , and fundamental resonant frequency (F_n) maps for Quaternary deposits.

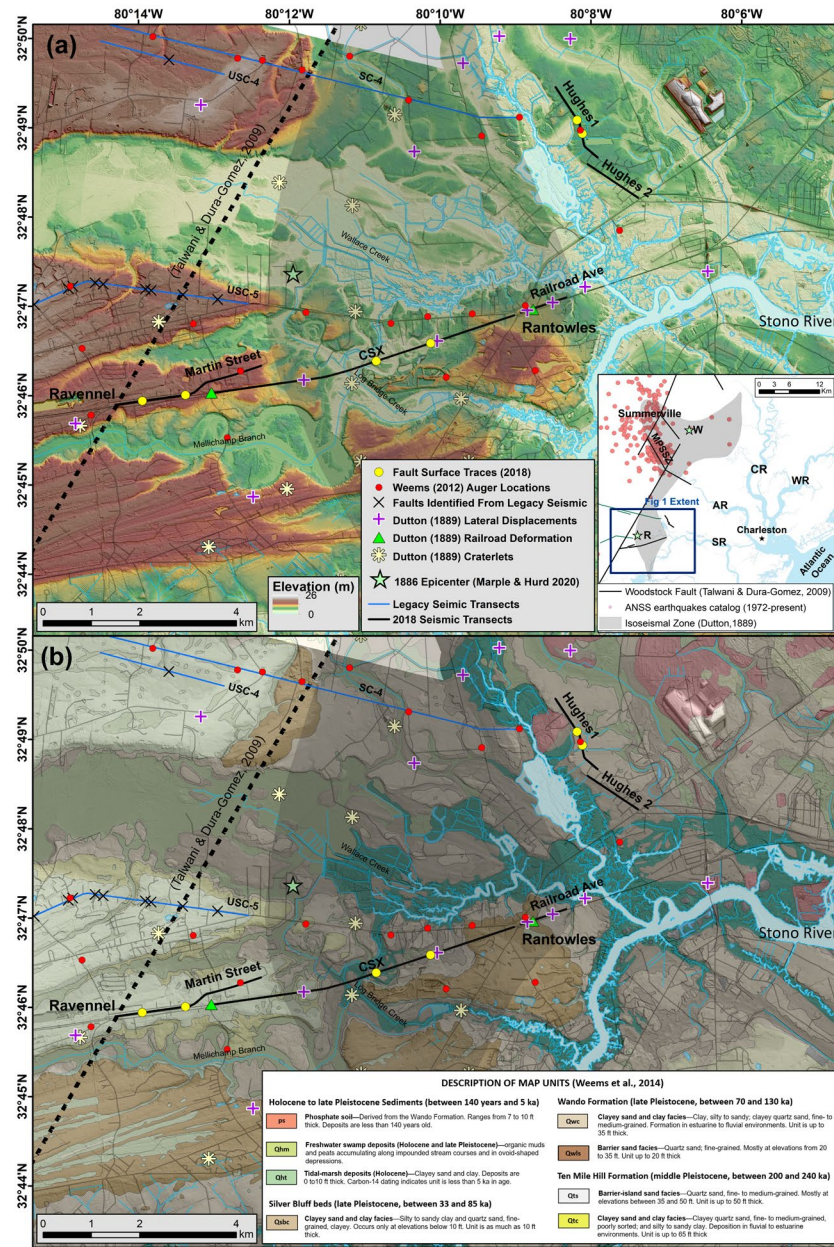


Figure 1. (a) Topographic map with seismic profile and Woodstock fault location (Talwani and Dura-Gomez, 2009) within the southern 1886 isoseismal region. Seismic profiles with fault locations (X and yellow circles) are Martin, CSX, Railroad, and Hughes 1 and 2 (black lines) and legacy seismic data (bluelines) are from Marple and Miller (2006). Also shown are surface deformation features (Dutton, 1889), boreholes (Weems et al. 2014), and Woodstock and Rantowles 1886 epicenter locations (Marple & Hurd 2020). The inset map shows the complete isoseismal region (Dutton in 1889) and earthquake epicenters. AR=Ashley River, SR=Stono River, CR=Cooper River, WR=Wando River (WR), MPSSZ=Middleton Place-Summerville Seismic Zone, S=Summerville. (b) Simplified surficial geologic map, modified from Weems et al. (2014) overlain on topography.

Geologic and Tectonic Setting

Charleston lies on the Atlantic Coastal Plain (ACP), an extensive region where seaward thickening of Cretaceous and younger open marine to fluvial sedimentary strata are deposited along a low elevation, low relief topography continental margin (Figure 1). The major lithofacies formed in fluvial-estuary-back barrier, barrier-island, and shallow-open marine shelf environments (Weems and Lemon, 2014). Weems and Lewis (2002) described the stratigraphy as more of a mosaic, rather than a simple layered sequence, namely due to the complex interactions between deposition, erosion, and tectonic warping over time.

ACP sediments formed from sea level transgressions during interglacial periods, and Pleistocene and younger deposits lie in the upper 10s of meters in the Charleston region. These sediments contain poorly consolidated, easily erodible sands and clays that unconformably overlie more competent Tertiary carbonate strata. This shallow high seismic impedance boundary has been shown to control site response at high seismic frequencies (e.g., Andrus et al., 2006; Chapman et al., 2006). Where high porosity saturated Quaternary sediments appear, liquefaction potential from strong ground shaking is elevated. To this point, ground displacements and liquefaction were regionally extensive during the 1886 earthquake (Dutton, 1889). Additionally, liquefaction evidence for several generations of prehistoric earthquakes have been found (Amick and Gelinas, 1991). Radiocarbon ages for these events document five prehistoric earthquakes in the Charleston Area, with approximate ages of 600, 1250, 3200, 5100, and older than 5150 years before 1991. The relationship between ground deformation, active faults and soil

properties is poorly understood, and this study seeks to expand our understanding of earthquake sources and ground amplification/liquefaction potential.

The Quaternary stratigraphy for the isoseismal region can be divided into seven major marine and fluvial units. Quaternary stratigraphy includes unnamed Holocene fluvial sediments deposited from modern rivers, late Pleistocene (33-85 ka) Silver bluff Formation, late Pleistocene (70-100 ka) Wando Formation, middle Pleistocene (200-240 ka) Ten Mile Hill Beds, middle Pleistocene (240-730 ka) Ladson Formation, early Pleistocene (730-1600 ka) Daniel Island Beds, and the early Pleistocene (730-970 ka) Penholoway Formation (Weems et al., 1987; Weems et al., 2014). These mechanically weak, Quaternary deposits directly overlie more competent Oligocene (29 Ma) calcarenite (detrital limestone) deposits of the Copper marl group, locally known as the Ashley formation (Weems et al., 1987; Weems et al., 2014).

Heidari and Andrus (2012) identified Ten Mile Hill, Wando, Silver Bluff, and Holocene deposits at ground displacement and craterlet sites that resulted from the 1886 earthquake (Figure 1). Out of the total of 51 craterlet and horizontal ground displacements observed, 49 are associated with late-middle Pleistocene strata. Notably, 23 ground failure sites are associated within the Ten Mile Hill beds. My study area offers an opportunity to expand the relationships of Heidari and Andrus (2012), as they conducted limited surveys within the southern epicentral region. Andrus et al. (2006) analyzed 91 cone penetrometer test (CPT) and seismic cone penetrometer test (SCPT) sites in the greater Charleston area to characterize in-situ V_s of these Quaternary and Tertiary deposits. They identified an extremely low range of V_s within Quaternary deposits, with little to no velocity-to-depth dependence and with V_s generally increasing

gradually with depositional age. One notable exception to these observations is within the Ten Mile Hill beds, where reworked sediments from 1886 ground shaking were suspected.

Figure 2 shows mapped faults in the study area, illustrating either a lack of agreement between past studies or a complex fault distribution throughout the 1886 epicentral region. From topography and stream gradient data, Marple and Miller (2006) mapped the East Coast fault, later termed the Woodstock fault, through the Ravenel and Summerville region (Figure 2a). This fault is consistent with 1) a region of modern seismicity termed the Middleton Place-Summerville Seismic Zone (Talwani and Dura Gomez, 2009; Chapman et al., 2016), 2) the 1886 epicentral region (Dutton, 1889), 3) an inflection in reflectors along seismic profile VT2 (Chapman and Beale, 2010), and 4) offset strata identified on COCORP C-2 profile (Chapman and Beale, 2008) and faulting identified by Marple and Miller (2006) along the USC-5 profile. Subsequent fault geometry revisions, based on a new catalog of seismicity and structural models, were presented by Talwani and Dura-Gomez (2009). Talwani and Dura-Gomez (2009) favored a left step in the dextral Woodstock fault (Figure 2b), over the 12° bend model presented by Marple and Miller (2006). The ~50 km long Woodstock fault system by Talwani and Dura-Gomez (2009) is mapped as a northeast-striking, northwest dipping, oblique-reverse right lateral strike slip fault with a ~6 km anti-dilation left step termed the Sawmill Branch Fault (Figure 1; Figure 2). The Sawmill Branch segment projects through the Summerville-Middleton Region, coinciding with the zone of modern seismicity, and connecting the north and south fault segments. Weems et al. (2014) presented a second Woodstock fault stepover model (Figure 2c) with major thrust faults

inferred from interpreted uplift bounding a series of smaller faults inferred from drill hole logs. However, Marple (2011) argued that the Woodstock Fault was not offset at some locations, favoring the previous interpretation of a slight eastward bend in the Woodstock fault as it crosses the Ashley River, over a significant left-step (Marple and Miller, 2006; Marple and Hurd, 2020). Other faults mapped in the region include the Adams Run fault, Charleston fault, Lincolnville fault, Ashley River fault, Summerville Fault, and Berkeley fault (Weems and Lewis, 2002; Marple and Miller, 2006; Talwani and Dura-Gomez, 2009).

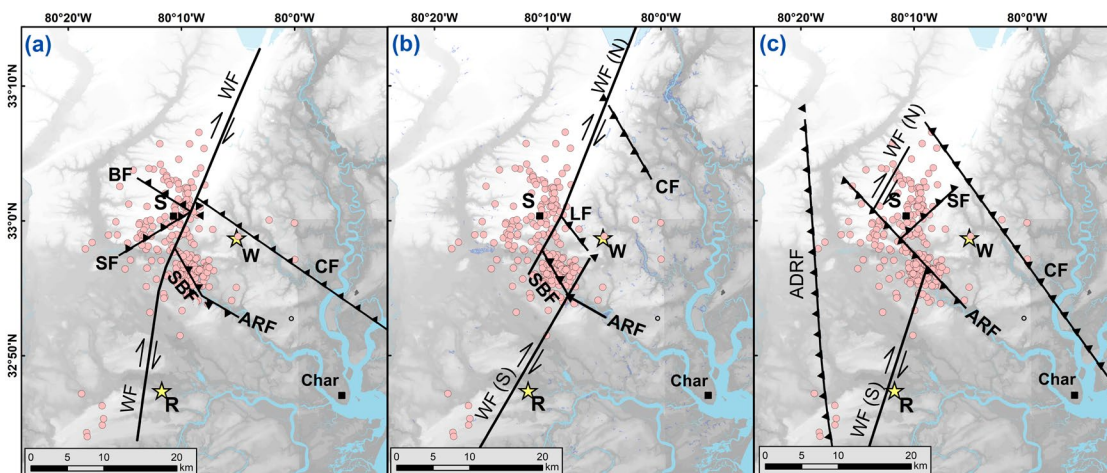


Figure 2. Fault interpretation for the greater Charleston region with earthquake epicentral locations: (a) Marple and Miller (2006) model of the Woodstock Fault (WF) as a continuous fault with a 12° fault bend; (b) Talwani and Dura-Gomez (2009) Woodstock fault stepover model; (c) Weems et al. (2014) Woodstock fault stepover model. S= Summerville; Char= Charleston. Yellow stars represent 1886 Woodstock and Rantowles epicenter locations (Marple and Hurd, 2020). Woodstock fault (WF), where N and S define the northern and southern fault strands in (b) and (c). SF=Summerville fault; ARF=Ashley River fault; SBF=Sawmill Branch fault; LF=Lincolnville fault; CF=Charleston fault; ADRF=Adams Run fault; BF=Berkeley fault. Earthquake locations from 1972 to present are from the U.S. Geological Survey (USGS) comprehensive earthquake catalog (U.S. Geological Survey, 2020).

Seismic Properties

For unconsolidated sediments, seismic velocities are strongly controlled by lithology, fluid content, and porosity (e.g., Mavko et al., 2009). Unsaturated Quaternary strata show V_p values ranging from 300 to 800 m/s (Odum et al., 2003; this study). Where saturated high porosity unconsolidated sediments are found, I typically observe V_p slightly faster than the speed of sound in water (between 1,500 to 1,600 m/s), providing the largest V_p impedance. The average V_p for ACP sediments typically range between 1,800-2,000 m/s (e.g., Odum et al., 2003; Chapman and Beale, 2010; Buckner, 2011) and the boundary between saturated Quaternary and Tertiary strata is not resolvable with refraction tomography approaches. Thus, I do not focus on V_p structure for my stratigraphic analysis. Because water saturation is a critical component to liquefaction, I rely on the depth to water saturation from borehole data (Gathro, 2018) and I use the elevation above sea level and regional river levels for a water saturation proxy. For a seismic constraint, I rely on independent estimate of depth to Tertiary strata from borehole data (e.g., Weems et al., 1987). Both saturated sediments and Tertiary bedrock mostly lie within the first 20 m below land surface in my study area, necessitating the need for near surface geophysical approaches to estimate shallow soil properties.

V_s is strongly tied to soil and rock stiffness and less dependent on fluid saturation when compared to V_p (Boore and Atkinson, 2008; Mavko et al., 2009). In the Charleston area, V_s for Quaternary strata generally ranges from 100 to 300 m/s, (e.g., Andrus et al., 2006; Chapman et al., 2006; Weems et al., 2014; Figure 3). V_s for the underlying top of Tertiary strata averages 417 m/s, with a standard deviation of 242 m/s (Andrus et al.,

2006; Chapman et al., 2006). Given the V_s impedance between 2 to 6 for the Quaternary to Tertiary transition, Chapman et al. (2006) identified this boundary as critical to assessing high frequency earthquake site response. Given this large V_s contrast at shallow depths, I utilize the multi-channel analysis of surface waves (MASW) active source seismic approach to extract V_s estimates from Rayleigh waves phase velocity dispersion. Seismic reflection surveys for the Charleston region have provided strong controls on Tertiary and younger strata (Marple and Miller, 2006; Chapman and Beale, 2008; Chapman and Beale, 2010). As a complementary dataset, I process and interpret reflection data in search of dip-slip motion along active faults of the region.

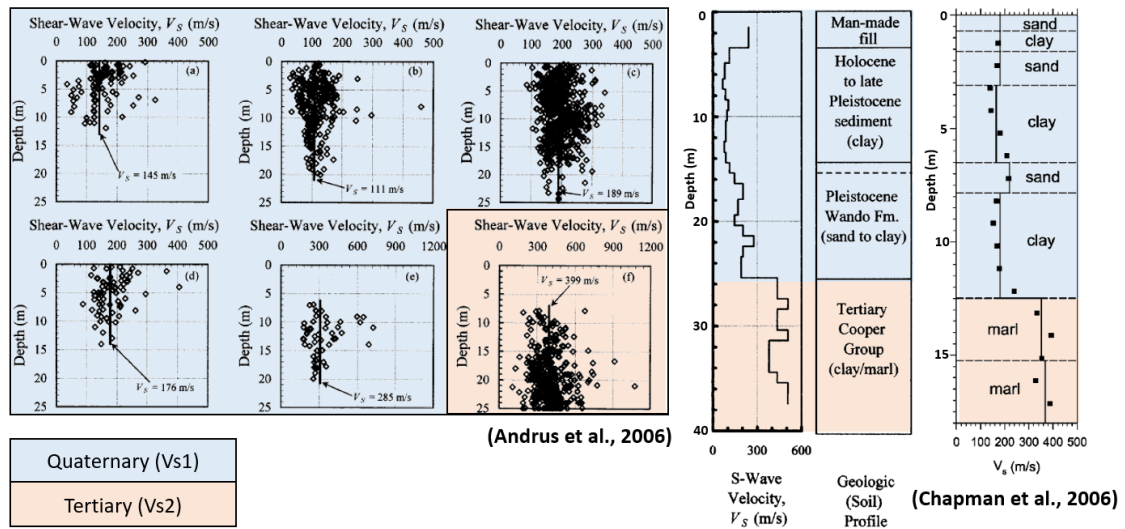


Figure 3. CPT-derived V_s (m/s) - depth (m) profiles with mean values for (a) Man-made fills, (b) Holocene and late Pleistocene deposits, (c) Wando Formation, (d) Ten Mile Hill beds, (e) Penholoway Formation and Daniel Island beds, and (f) Tertiary deposits (modified from Andrus et al. 2006 and Chapman et al. 2006). Quaternary strata (blue) and Tertiary strata (tan).

CHAPTER TWO: DATA AND METHODOLOGY

Data

In April 2018, a Boise State University crew acquired about 14 km of new land streamer seismic data in the vicinity of the southern isoseismal region of the 1886 earthquake (Figure 1). These data cross mapped traces of the Woodstock and related faults that have been identified as Quaternary active. The surveys also cross several notable 1886 ground failures (Dutton, 1889). The land streamer seismic data were acquired at 2.5 m shot spacing using a 50 kg hitch-mounted accelerated weight drop source and 72 vertical-component, 10 Hz baseplate-coupled geophones spaced at 1.25 m with the nearest channel spaced 5-m from the source. The geophones were embedded in fire hose and tethered to the source and vehicle. This survey utilized a differential GPS system to obtain accurate position measurements during data collection with a decimeter-precision odometer mounted to the source vehicle to provide accurate source positioning. Data were collected at a rate of 2-4 km per day. Some seismic profiles were obtained with the assistance of a certified road survey crew to control traffic both along city streets and along the CSX rail access road. The source produced broad-band signals between 5-300 Hz and the survey yielded over 5,300 shot gathers with a 90 m aperture over the receiver array. From this dataset I pick fundamental mode Rayleigh wave phase velocity dispersion curves to develop V_s models, and I use reflection signals to map stratigraphy 500 meters below land surface (Figure 4).

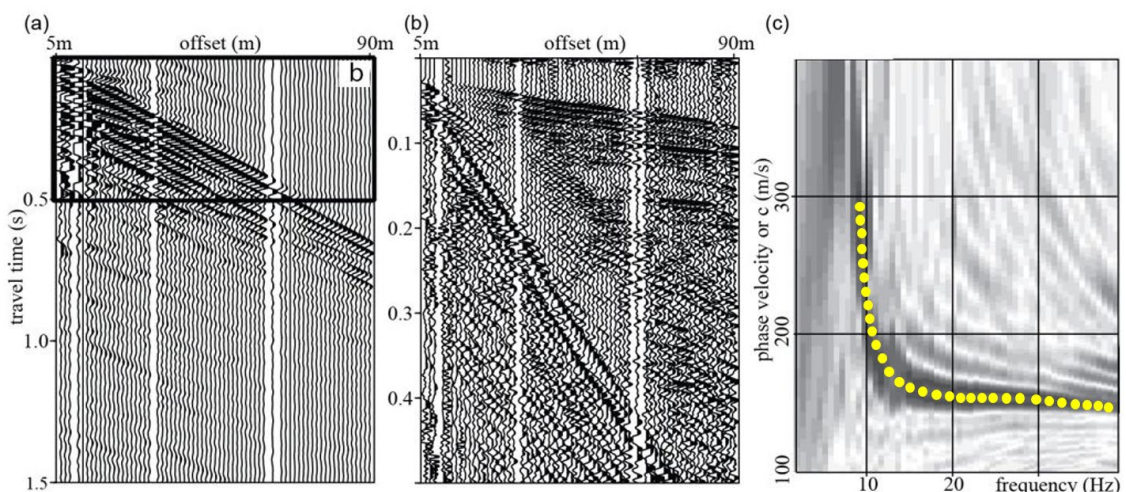


Figure 4. (a) Unprocessed field record 8420 from Railroad Ave showing low-velocity surface waves that dominate the wavefield. (b) Filtered (30–200 Hz) field record of (a), confirming soil saturation from 1500 m/s first-arrival wave speed. (c) Dispersion image from (a). I pick the fundamental mode of the Rayleigh wave (indicated by yellow points on panel (c)). Figure 5 revised from Liberty et al. (2021).

Vs Derived from Surface Waves – Grid Search Approach

I pick fundamental Rayleigh wave dispersion through a multi-channel surface wave (MASW) approach (Park et al., 1999; Xia et al. 1999). I use code developed at Boise State University to pick fundamental mode Rayleigh wave dispersion (e.g., Mikesell et al., 2017). Through sensitivity tests, dispersion curve characteristics and results from previous studies, I limit my Rayleigh wave inversions to only two-layer model solutions through a grid search approach (Andrus et al., 2006, Liberty et al., 2021). I show that my lowest picked frequencies are more dependent on local site conditions and less on seismic source and receiver capabilities. The low frequency fundamental mode surface wave cut-off is summarized in Xia et al. (2006), and when combined with previous surface wave studies for the region, reinforces simple model solutions for this geological environment. The highest frequencies that I pick lie on the flat portion of the dispersion curve, where the surface waves only probe the upper layer. This Rayleigh

wave speed asymptote directly relates to the upper layer properties and provides late Quaternary V_s (V_{s1}) values with high confidence (Liberty et al., 2021).

From dispersion characteristics and V_s distributions of Andrus et al. (2006), I obtain a range of one-dimensional V_s solutions by generating fundamental mode dispersion curves for a range of plausible models (Michaels and Smith, 1997; Michaels, 2018). I then compare calculated phase velocities for the range of observed frequencies to obtain the best-fit V_s model for each shot gather. I produce upwards of 41,000 forward models and choose the model that minimizes the misfit between observed and calculated dispersion picks (Liberty et al., 2021). Although V_s is the dominant control on Rayleigh wave speeds, bulk density and V_p are needed to generate my forward models. Bulk density estimates for my models were obtained from nearby measurements of Andrus et al. (2006) and compared to the global empirical measurements of Boore (2016). I run models for both saturated and unsaturated upper layer conditions using V_p estimates from my first arrival analysis. I use only the saturated model results to generate my profile and regional maps, as they produced a better fit to control points where borehole data (Weems et al., 1987) align with my seismic measurements. However, I explore the dry soil model solutions in my discussion. Since the lower layer Tertiary strata in my study area mostly lie below sea level, and regionally the water table depth is ~ 3 m below the surface on average, I assume the lower Tertiary layer is fully saturated. I generate models using an upper layer V_s that is controlled by the range of measured high frequency Rayleigh wave phase velocities and a range of realistic Poisson's ratio values for unconsolidated sediments (Liberty et al., 2021). This results in a step size for V_{s1} of about 1 m/s over 15 upper layer V_s solutions. For my lower layer or Tertiary V_s (V_{s2}), I

run models from 250 to 800 m/s with a step size of 25 m/s. I model boundary depths from 0.25 to 20 m at a 0.25 m step size. All of these Vs and depth ranges are consistent with end-member downhole measurements of Andrus et al. (2006) and Weems et al. (1987), and my final models lie well within these ranges. As a measure of uncertainty, I fit additional solutions that measure +/- 10 m/s for each picked frequency. A summary of model parameters and constraints are shown in Table 1.1.

Table 1.1 Unsaturated and saturated grid search model parameters. Vp (upper and lower layer) and lower layer Vs units are m/s, Vs1 unit is a percent scalar of the Rayleigh-wave phase velocity, density (ρ) units are kg/m³, and depth unit is meters.

Model	Vp1	Vp2	Vs1 Range as % scalar of phase velocity	Vs2 Range	ρ 1	ρ 2	Depth Range at 0.25 m step size
Dry	365-700	1740	0.91:01:1.05	250:25:800	1590	1886	0.25:0.25:30
Saturated	1497-1600	1740	0.91:01:1.05	250:25:800	1855	1886	0.25:0.25:30

I analyzed 5,000 individual shot gathers, from which 2,718 high quality fundamental mode surface wave picks were incorporated in my final models. My two-layer, one-dimensional model solutions yield an average root mean square error of about 2 m/s, as measured by an average Rayleigh wave speed difference for each picked frequency. Coincident borehole measurements validate my final models (Weems et al., 1987; Figure 1). I note that my models are less sensitive to lower layer Vs (Figure 5). This results from limited surface wave energy that probes this lower layer and due to the mode kissing phenomena (interaction of higher modes with the fundamental mode at low frequencies) (Gao et al., 2016). Although this lower layer Vs value is not needed to

estimate F_n , it is required to estimate seismic impedance. I note that my impedance estimates are less well constrained compared to upper layer V_s and boundary depth.

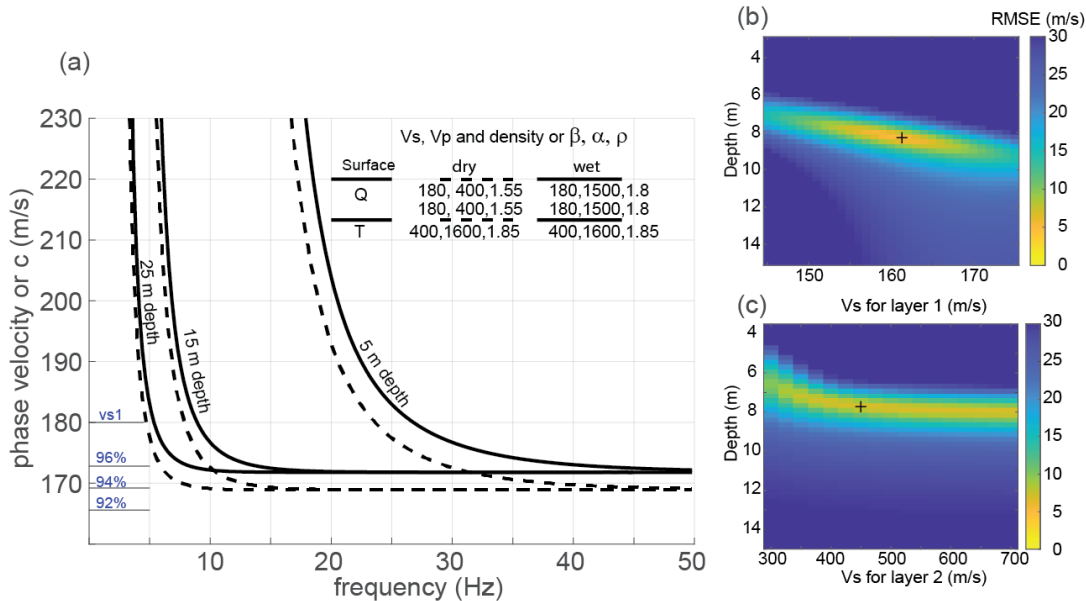


Figure 5. (a) Fundamental mode dispersion curves for two-layer over half-space models. These models represent 5, 15, and 25 m of Quaternary sediments over Tertiary sedimentary bedrock. Velocities and densities are in m/s and g/cc units, respectively. Dashed lines represent dry soil over bedrock models, whereas solid lines represent saturated soils over bedrock models. (b) RMS error distribution for all upper layer V_s -layer thickness models. (c) RMS error distribution for all lower layer V_s -upper layer thickness models. The black cross on (b) and (c) denotes the global minimum solution.

I assign each best-fit model to the geophone aperture midpoint for each shot gather. I generate final 2-D models by combining individual 1D inversion results along each profile, and smoothing with a 35-sample median filter. I describe my V_s results using the National Earthquake Hazard Reduction Program (NEHRP) site classifications for both field and modeled data (Building Seismic Safety Council [BSSC], 2009). I then generate an estimate of high frequency site response, in profile, using equation 1, the quarter wavelength relationship ($F_n = V_{s1}/4h$) of Shearer and Orcutt (1987), where V_{s1} is the upper layer V_s , and h is the upper layer thickness. Furthermore, I compare my V_s

models to borehole measurements (Andrus et al., 2006; Heidari and Andrus, 2012; Gathro, 2018), surficial geology (Weems et al., 2014), and empirically derived density measurements (Boore, 2016).

Sensitivity Analysis

To validate my modeling approach, I compare my two-layer grid search output to a standard 10-layer deterministic inversion approach (Surfseis, ®). I compare two grid search output models (saturated and unsaturated) to the Surfseis model with the default Poisson's ratio and density values. I use the dispersion picks from a shot close to borehole RA-16. This borehole located about 300 m to the north of my Railroad profile, shows approximately 6.7 m of Wando Formation deposits over Tertiary Ashley strata (Figure 6; Weems et al., 1987). All three models identify an abrupt boundary near the top of Tertiary depth identified in the borehole. However, the top of Tertiary from RA-16 best matches the saturated grid search output. Furthermore, my saturated model lower layer Vs (Vs2) best matches the Tertiary formation averages of Andrus et al. (2006).

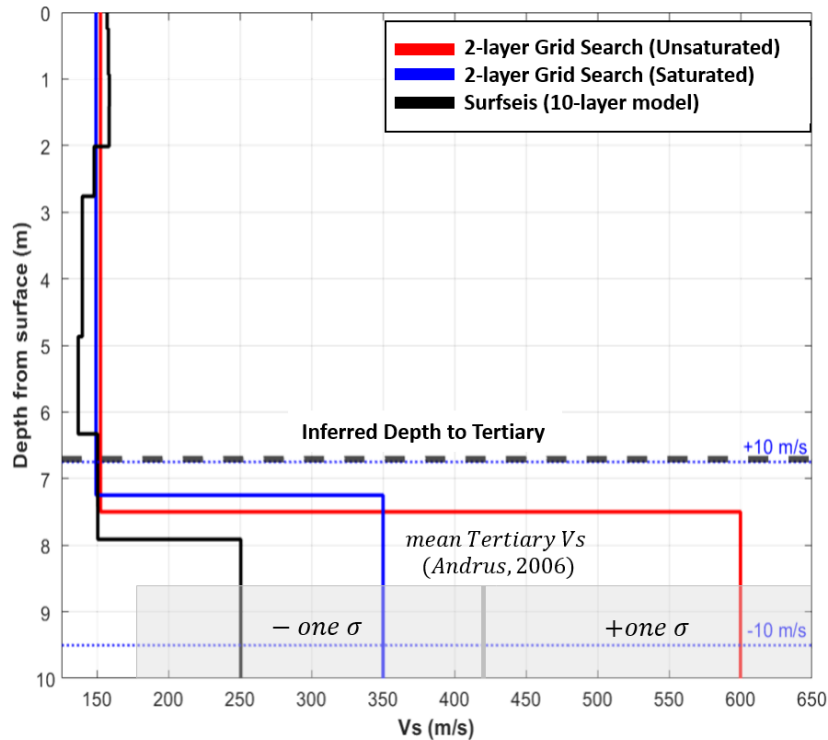


Figure 6. Vs-depth profiles near borehole RA-16. Saturated (blue line) and unsaturated (red line) best-fit two-layer models, 10-layer deterministic Surfseis model (black line), and depth to Tertiary at RA-16 (black dashed line). Best fit, two-layer saturated model solutions using +/- 10 m/s dispersion picks (blue dotted lines) and +/- one standard deviation from the mean value of Tertiary (gray rectangle) are from Andrus et al. (2006).

Reflection Profiling

Because surface waves tend to dominate the recording systems dynamic range at low wave speeds, I extract coherent reflections only between first arrival head waves and the dominant Rayleigh wave signals (Figure 4). This reflection window has been termed the “optimum window” (Hunter et al., 1984) and for shallow, limited aperture seismic surveys, this window contains reflection signals that are not contaminated with surface waves. In the presence of saturated unconsolidated/semi consolidated sediments, the optimum window allows robust velocity analyses for the upper ~500 m depth for my offset range.

I processed the reflection data using Halliburton's SeisSpace® ProMAX® seismic processing software with a standard processing approach outlined by Yilmaz (2001). Geometry was applied to each source and receiver location from differentially corrected GPS positions recorded at each shot record. Processing steps included datum statics, spiking deconvolution, bandpass filter, surface wave attenuation through a two-step singular value decomposition approach to estimate and adaptively subtract the ground roll signal (where appropriate), iterative velocity analyses with dip moveout corrections, amplitude gains, and a post-stack time to depth conversion. Where surface waves were strong, I muted this window. Post-stack migration is selectively applied to the data where appropriate so as to not introduce migration artifacts which can distort key reflector geometries. Depths were estimated using 1-D averaged stacking velocity models. These velocities were consistent with measurements of the regional seismic profiles of Buckner (2011).

CHAPTER THREE: GRID SEARCH AND REFLECTION PROFILING RESULTS

Railroad Avenue Seismic Profile

The one km long, west to east Railroad Avenue seismic profile extends from Hwy 162 at Rantowles to the eastern road termination at a foot bridge near Wallace Creek (Figure 1). Weems et al. (2014) mapped late Pleistocene Wando Formation sands and clays along the profile. Auger hole RA-16, drilled near the western limits of the profile, provides depth to Tertiary constraints. Dutton (1889) identified two lateral displacement features from the 1886 earthquake, adjacent to the rail line along this transect (locations obtained from Heidari, 2011). The water table, determined from nearby water wells, lies just above sea level.

I picked Rayleigh wave dispersion between about 10-40 Hz, allowing V_s estimates to about 10 m depth (Figure 7). For my final V_s models, I calculate an average misfit of 1.4 m/s between observed and calculated fundamental dispersion curves. My models indicate that the upper layer late Quaternary Wando Formation V_s ranges from 131 to 175 m/s, consistent with in situ downhole measurements (Andrus et al., 2006). I estimate a mean velocity of 154.7 m/s and a standard deviation of ~10 m/s. The Quaternary thickness, or depth to the high impedance boundary formed by the underlying Tertiary strata, ranges from 5 to 8.75 meters. This surface undulates upwards of a few meters over a lateral scale of hundreds of meters, consistent with a fluvial-estuarine depositional environment. My best fit models estimate a mean Tertiary V_s of 529 m/s with a standard deviation of ~161 m/s. This, too, is consistent with the insitu

measurements of Andrus et al. (2006). I classify the Wando Formation strata as NEHRP Class E soils (<180 m/s) and top of Tertiary strata as NEHRP Class C and D soils (180 to 760 m/s). On Railroad Ave I estimate a Vs impedance at the Quaternary-Tertiary boundary that ranges from 2 to 5 and a Fn that ranges from 5 to 7 Hz. The lateral displacement locations of Dutton (1889), while poorly constrained in space, are consistent with high impedance, low upper layer Vs zone.

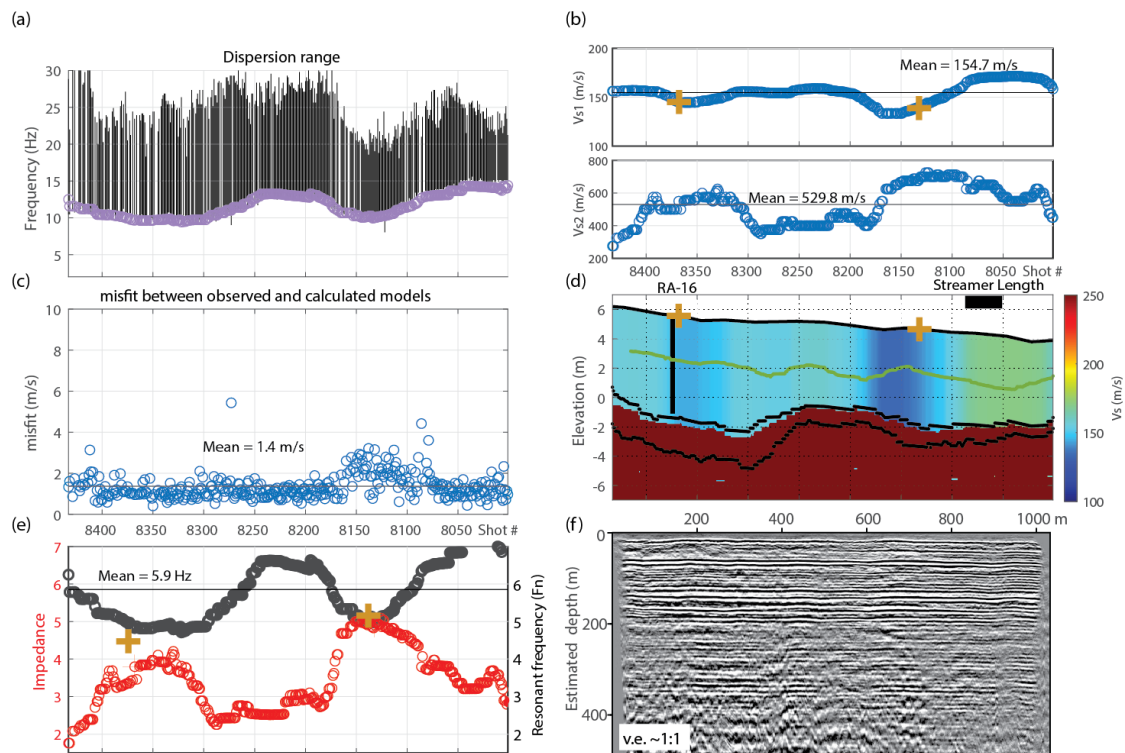


Figure 7. Two-layer best fit model for the one-km long Railroad profile. Horizontal axis is in shot gathers with consecutive shot gathers spaced 2.5 m apart. (a) Picked dispersion frequency range (black lines), with the estimated cutoff frequency of Xia et al. 1999 (purple points). (b) Quaternary (Vs1) and Tertiary (Vs2) layer Vs velocities. (c) Model misfit (difference between observed and calculated). (d) 2-layer shear wave velocity model from 433 1-D best fit models. Green line indicates water table elevation from refraction analysis. The black vertical line indicates the location and depth to Tertiary strata encountered in borehole RA-16. Horizontal black lines indicate the resulting depth to Tertiary for phase velocity perturbation of +/- 10 m/s applied to dispersion picks. Black rectangle (top right) indicates the length of the geophone array. (e) Resonant frequency yellow and impedance (blue) along the transect. (f) Reflection cross section from this transect in the upper 500 meters. The location of lateral displacements mapped by Dutton in 1889 (red crosses).

I identify reflections to about 0.4 s two-way travel time, or about 0.4 km depth (Figure 7f). I observe strong amplitude flat lying continuous reflectors in the upper few hundred meters, suggesting no faults with measurable vertical displacements cross this profile. My observations suggest that the deformation that resulted from the 1886 earthquake was not generated from motion along a fault that lies beneath the Railroad profile.

Martin Street and CSX Seismic Profiles

The 3.15 km west to east Martin profile begins immediately east of the Ravenel rail station and terminates at the eastern termination of Martin Street (Figure 1). The 6.55 km west to east CSX profile extends the Martin profile to the east, along a railroad access road. Dutton (1889) identified the central portion of the CSX profile as within the southern epicentral (or isoseismal) region of the 1886 earthquake (Figure 1). Dutton identified lateral displacements, liquefaction craterlets, rail line deformation (Figure 1). Weems et al. (2014) mapped mostly middle Pleistocene sands of the Ten Mile Hill formation along the length of the Martin profile and Pleistocene sands and clay-rich sand deposits of the Wando, Silver Bluff and Ten Mile Hill formation along most of the CSX profile. At lower elevations in the center of the CSX profile, Weems et al., (2014) identified outcrops of Holocene-age Freshwater swamp and Tidal-marsh deposits.

The northeast-trending Woodstock fault may cross near the west of the Martin profile (Marple and Miller, 2006; Talwani and Dura-Gomez, 2009; Weems et al., 2014; Figure 1), but the closest location constraint is from the seismic profile USC-5, located about two km to the north (Figure 1). Here, based on offset reflectors, Marple and Miller (2006) documented a ~5 km wide deformation zone that presumably extends to the north

and south. A number of boreholes lie close to these profiles (Weems et al., 1987), providing comparisons for my depth to top of Tertiary models.

I observe a mean misfit between observed and calculated values of 2.1 m/s for the Martin profile and a mean misfit of less than 3 m/s for the CSX profile (Figure 8). I attribute the higher CSX misfit to the poorer geophone coupling along the loose gravel of the railroad access road. My Rayleigh wave inversions place upper layer Vs between 144 and 198 m/s with an average Vs=167 m/s for the Martin profile (Figure 8). For CSX, Vs values range between 107 and 205 m/s with an average Vs=143 m/s. My Vs average is slower than the 184 m/s Vs average measured by Andrus et al. (2006) for the Ten Mile Hill formation (Table 1.3), but my values mostly fall within one standard deviation (54 m/s) of their measurements. I estimate average depth to top of Tertiary strata of 11.7 m with a range from 7 to 18.5 m for the Martin profile, consistent with boreholes RA-3 and RA-18 (Weems et al., 2014). For the CSX profile, I constrain the Quaternary thickness to between 4.5 and 14.5 meters, with an average depth to top of Tertiary of 7.8 m. These measurements are consistent with boreholes RA-39, RA-40, and RA-6. Fn average for the CSX profile is 4.7 Hz with a range from 2.9 to 7.3 Hz. I measure a mean Vs for Tertiary strata of 369 m/s for the Martin profile and 415 m/s for the CSX profile, consistent with Andrus et al. (2006) downhole measurements.

My calculated Quaternary to Tertiary impedance measures between 1.5 and 6.5, with an average impedance of 2.9. This suggests amplification from earthquake waves similar to that from the base of the Atlantic Coastal Plain sediment base (Chapman et al., 2006). Fn average for the Martin Street profile is 3.7 Hz with a range from 2.5 to 5.5 Hz.

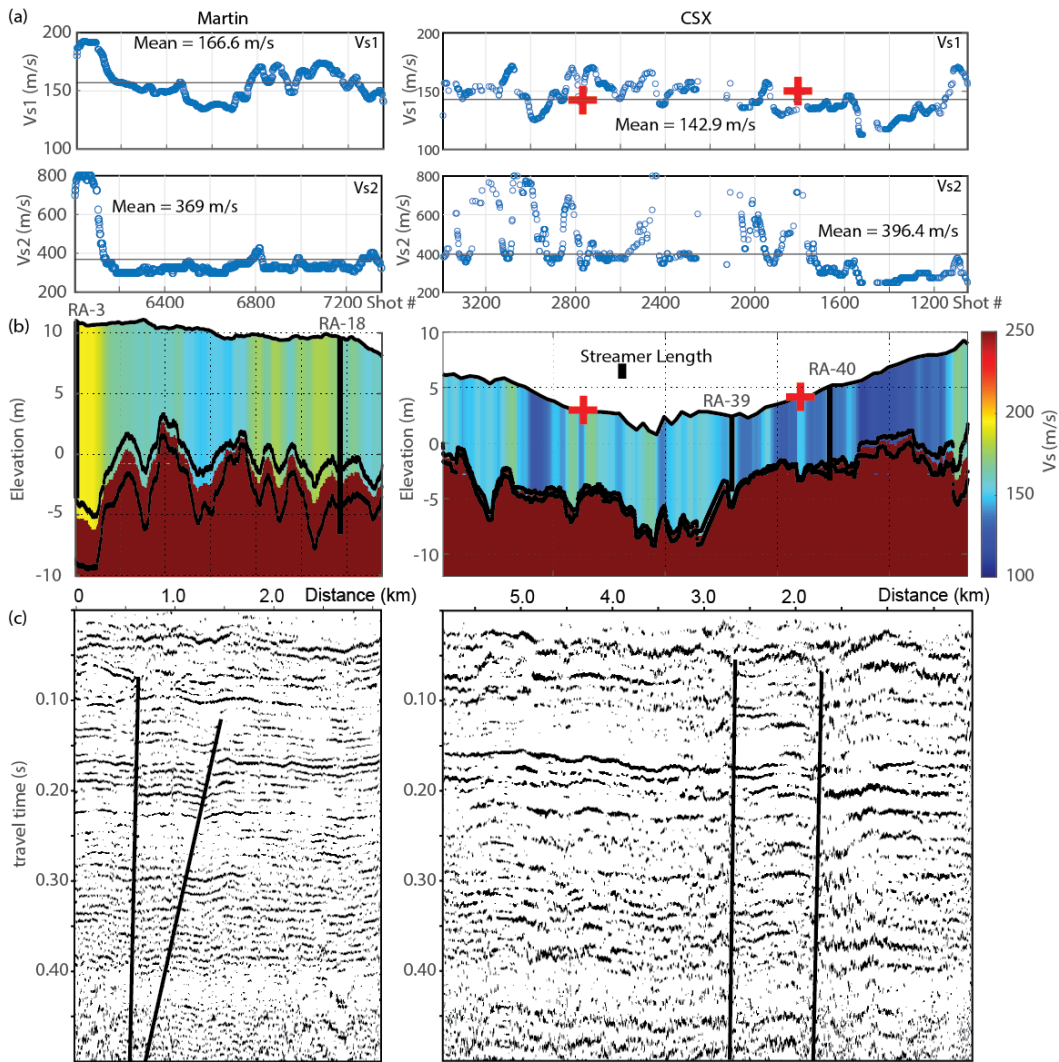


Figure 8. (a) Vs1 and Vs2 best fit solutions for Martin and CSX profiles. Horizontal axis is in shot gathers with consecutive shot gathers spaced 2.5 m apart. (b) 2-layer best fit Vs models for Martin and CSX profiles. The location of lateral displacements mapped by Dutton in 1889 (red crosses), land streamer length, and borehole constraints (black vertical lines) are shown. (c) Composite reflection cross section with ~8:1 vertical exaggeration for Martin and CSX in two-way travel time(s). Interpreted faults on (c) are indicated by black lines.

I observe reflections to more than 0.4 s two-way travel time or more than 300 m depth (Figure 8). I observe mostly flat-lying reflectors along the Martin Street profile, with offset and tilted reflectors within an 800 m wide zone between 0.8 to 1.6 km distance. For the CSX profile, I observe mostly flat-lying reflectors, with a change in seismic character between 1.7 to 2.7 km distance. Between this zone, I interpret two

faults that form a broad fold. This anticline lies within the isoseismal region (Figure 1) and close to lateral spread deposits identified by Dutton (1889). Although I do not identify significant stratigraphic offset, I define two faults that separate a km-wide zone of deformed strata. From reflector truncations, I identify faults that dip from 60-90 degrees.

Hughes Road Seismic Profile

The 2.6 km northwest to southeast Hughes Road (state road 10-738) profile consists of two segments (Figures 1). The northern segment extends from the road termination at a private residence southeast to a bend in the road and along the length of Dawning Lane. The southern segment begins on a private driveway and extends to the southeast to the Hwy 17 intersection. Approximately 6 m of elevation change is observed along this profile. Weems et al. (2014) mapped Pleistocene clays and sands of the Wando formation and Silver Bluff formation along the length of the profile (Figure 1). From my grid search model, I measure higher Quaternary V_s values along the northern segment of Hughes Road (mean $V_s=167$ m/s) compared to the southern segment (mean $V_s=145$ m/s) related to a lithologic transition from the Wando formation to north to the younger Silver Bluff formation to the south. Weems et al. (1987) identified the depth to Ashley River Tertiary strata at 2.7 m depth at auger hole RA-20 (Figure 9). The highest resonant F_n that I measure from my study area occurs along the Hughes profile where Quaternary strata is estimated as thin as 3 meters and on average is ~ 4.3 m in thickness. Chapman and Beale (2010) connect a northeast-trending fault identified on seismic profiles SC4 and C2 to extend across this profile. Dutton (1889) did not identify lateral displacement or craterlets along this profile (Figure 1).

The migrated, depth converted reflection stack shows mostly flat-lying reflectors to more than 0.6 km depth (Figure 9). A 0.3 km wide zone near 1 km distance shows a step down in lower amplitude reflectors indicates the presence of faulting on this profile. Fundamental resonant frequency along the length of the profile ranges from 10-20 Hz. This frequency content is higher than that measured along the CSX and Railroad profile and is consistent with a thin layer of Quaternary sediments over Tertiary strata. Ongoing V_p and V_s analyses will relate shallow properties to the dominant surface wave frequency.

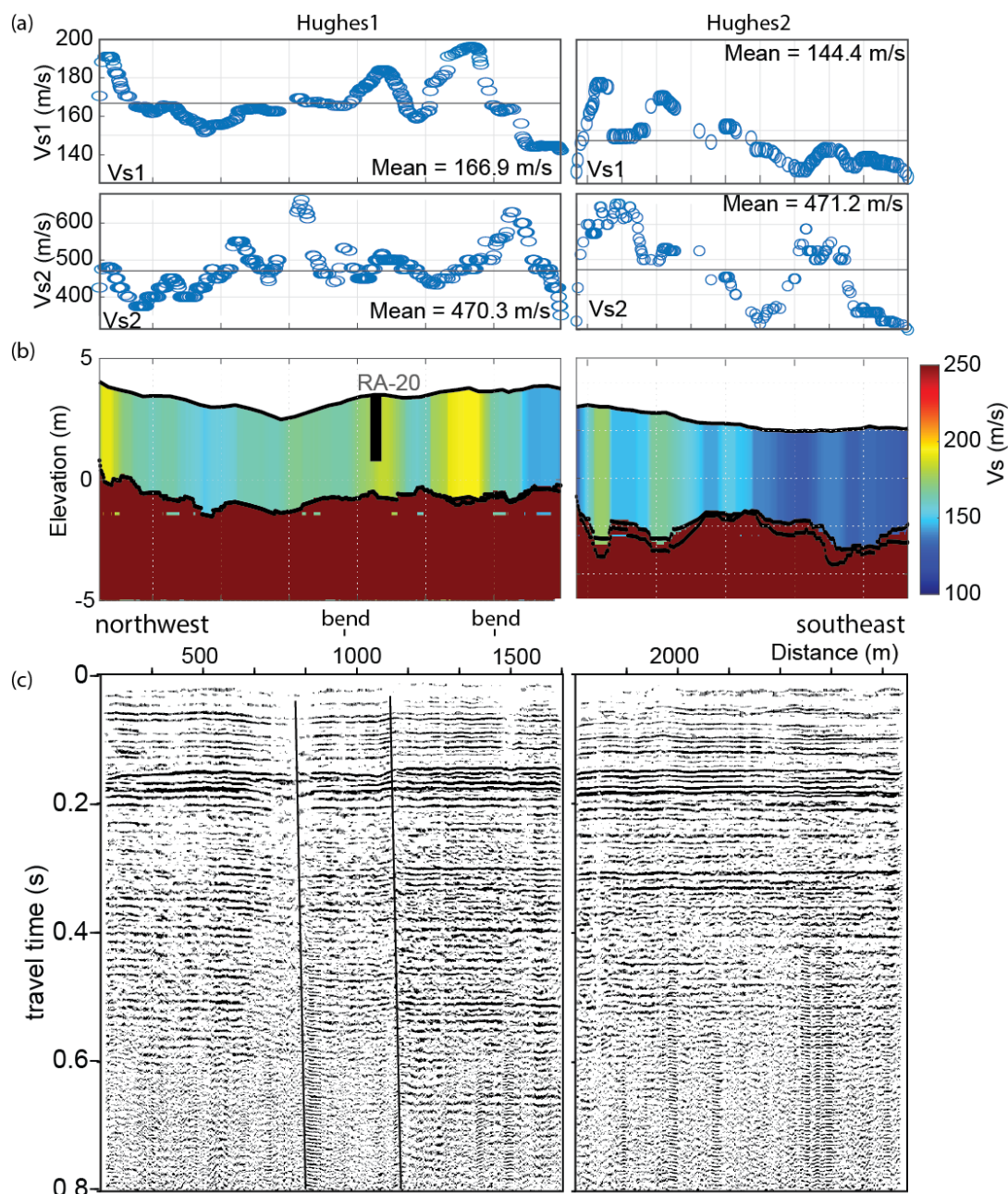


Figure 9. (a) Vs1 and Vs2 best fit solutions for Hughes 1 and 2. Horizontal axis is in shot gathers with consecutive shot gathers spaced 2.5 m apart. (b) 2-layer Grid Search Vs models for Hughes 1 and 2. Borehole constraints for depth to top of Tertiary strata from RA-20 is shown (b). (c) Composite reflection images with ~3:1 vertical exaggeration in estimated depth. Interpreted faults on (c) are indicated by black lines.

CHAPTER FOUR: DISCUSSION

Vs Comparisons to Lithology

I examine statistical properties of my Vs database following the methods of Weems et al. (2014), and group the data by lithology. My four profiles place Quaternary Vs between 107 and 208 m/s, with a mean of 156 m/s and a standard deviation of 17.5 m/s (Table 1.2). Lower Vs values typically signify loose clay, mud, and peat rich Holocene deposits, while the slightly higher Vs values generally represent older, more competent, more stiff or more sandy Pleistocene units such as the Wando and Ten Mile Hill units. Notably, 92.5 % of my Quaternary strata are classified as NEHRP E Class soft soils ($V_s < 180$ m/s). I summarize my bulk statistics for these formations, and I group the youngest Pleistocene unit, the Silver Bluff beds, with the Holocene units on the basis of age and subtle differences in Vs (Table 1.2). I also compare my measurements to those of Andrus et al. (2006) in Table 1.3 and Figure 10.

Table 1.2 Saturated 2-layer Grid Search Model Statistics.

Map Symbols	Unit	No. of Values	Mean Vs (m/s)	Max Vs (m/s)	Min Vs (m/s)	Standard Deviation (m/s)	Mean RMSE (m/s)
Qhm Qht Qsbc	Bulk Holocene-Late Pleistocene	515	144	205	107	15	3
Qwc Qwls	Bulk Wando Fm	995	159	208	118	15	2
Qtc Qts	Bulk Ten Mile Hill Fm	1208	158	198	111	19	2
Pa	Ashley Fm	2718	437	800	250	159	2
*	All Quaternary Units	2718	156	208	107	18	2

Table 1.3 CPT Statistics (Andrus et al. 2016).

Map Symbol	Unit	No. of Values	Mean Vs (m/s)	Standard Deviation (m/s)
Qhm Qht Qsbc	Holocene-Late Pleistocene	238	116	45
Qwc Qwls	Bulk Wando Fm	538	195	47
Qtc Qts	Bulk Ten Mile Hill Fm	73	184	54
Pa	Ashley Fm	383	417	242
*	All Quaternary Units	*	*	*

The relative density histogram for all Vs Quaternary deposits is close to normally distributed (Figure 10d). I note that more than 99% of my Holocene Vs measurements

fall within +/- one standard deviation of the Andrus et al. (2006) downhole Vs results. This value is reduced to 85.2 % if the late Pleistocene Silver Bluff beds are included. Greater than 75% of my Vs values for the Wando formation, >89% of Ten Mile Hill, and > 86% of observations on Tertiary deposits fall within +/- one standard deviation of the mean Vs value reported by Andrus et al. (2006) for the respective units. Similar to Andrus et al. (2006), I do not observe a statistically relevant increase in Vs with deposit age. This suggests no age/diagenesis relationship for these soils (Obermeier, 1996). Besides from measurements where Ten Mile Hill beds are mapped (Gathro, 2018). I do however observe a consistent relationship between Vs and Quaternary thickness. I note lower Vs in the older Ten Mile Hill beds than the younger Wando Formation, and observe a significant Vs-depth gradient in the Ten Mile Hill Formation (Figure 10c) of ~3-4 m/s per meter, suggesting that a gradient model may be more appropriate for this lithology.

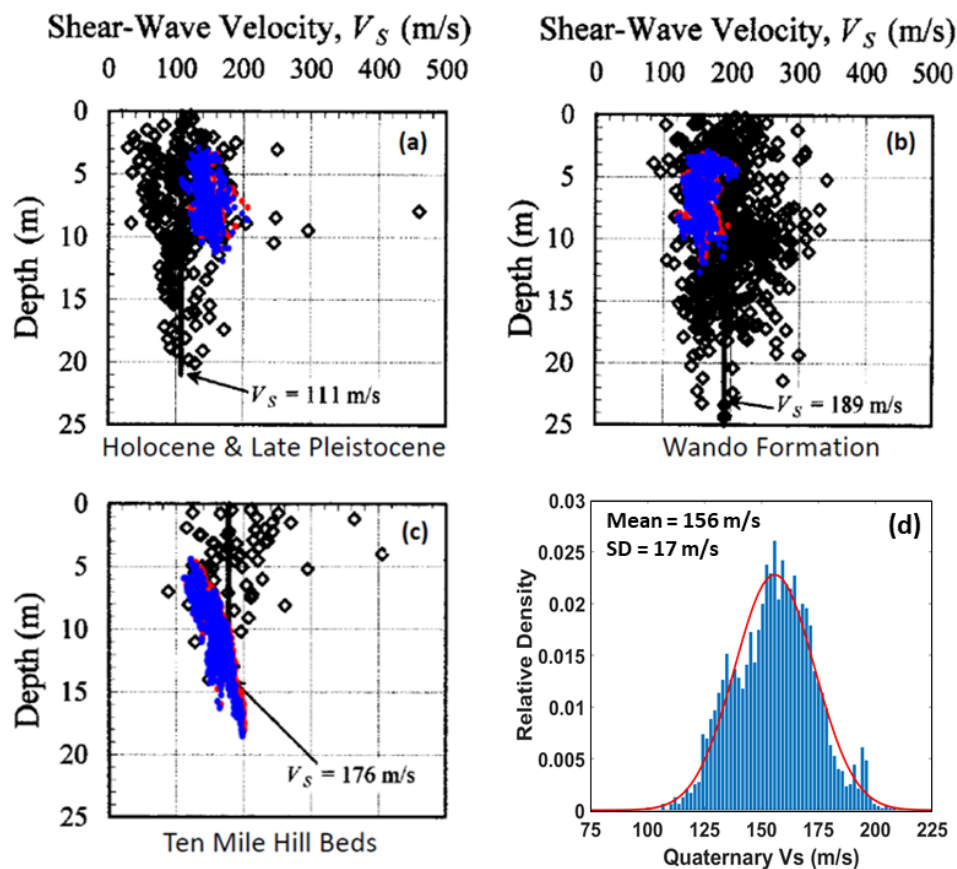


Figure 10. V_s -depth plots for three lithologies. Andrus et al. (2006) CPT data (black circles), MASW V_s best fit models for fully saturated (blue circles), and unsaturated (red circles). Black line and V_s value labeled on plots indicates median V_s values from CPT data. (a) Holocene-Late Pleistocene (units Qhm, Qht, & Qsbc), (b) Bulk Wando Formation (units Qwc and Qwls), (c) Bulk Ten Mile Hill Beds (units Qtc and Qts). (d) relative density histogram for V_s for all Quaternary units from this study with a theoretical normal distribution overlain (red line). The mean and standard deviation are shown.

Figure 10 shows my saturated and unsaturated V_s results compared to V_s -derived from in situ CPT measurements (Andrus et al., 2006). My results for both saturated and unsaturated model end members are consistent with the CPT data. I also note that a constant V_{s1} with depth for Holocene and Wando appear to be appropriate, but a 2-3 m/s V_s gradient model best fits Ten Mile Hill. The saturated and unsaturated end member models have a mean difference in V_{s1} of < 2 m/s, < 50 m/s for V_{s2} , and < 0.25 m in Quaternary thickness, and show a mean difference in RMSE of 0.257. I report the results

for the saturated model on the basis of very shallow groundwater table depth of typically less than 3 meters within the Charleston Region (Andrus et al., 2006; Gathro, 2018), with respect to the thickness of Quaternary sediments in the area, meaning the majority of the Quaternary strata is below the water table.

High frequency F_n Derived from Soil Thickness and V_s

I calculate F_n for each V_s measurement location using equation 1, where F_n relies only on V_{s1} and layer thickness. Given the low variability in Quaternary V_s within my study region, F_n appears to be mostly dependent on Quaternary thickness. Figure 11 demonstrates that I capture a well-distributed range of Quaternary thicknesses from 3-19 m. Given the relatively narrow range of V_s for my study area, I conclude that F_n for the southern Isoseismal zone ranges from 3-12 Hz. This suggests that from high frequency F_n , 1-3 story buildings would be the most vulnerable structures to strong ground motions (Arnold, 2006).

Figure 11 shows that I identify Ten Mile Hill beds that range in thickness from 4.5 to 18.5 m, leading to the lowest F_n measurements in my study area. Holocene and Silverbluff layers generally measure between 4 to 11 m thick, producing F_n that ranges from about 3 to 11 Hz. The Wando Formation displays a bimodal distribution of thickness, leading to the same bimodal F_n distribution. This is likely from my limited spatial sampling within this formation.

Within my study region, Quaternary thickness is a more significant driver of F_n than V_s , this is because the V_{s1} range is relatively discrete, on the order of about 100m/s, regardless of lithology, while Quaternary thickness in this region ranges from about 3-18 meters. I fit a power law function to my data (equation 2: $F_n = 69.64h^{(-1.568)} + 1.996$) to

establish a F_n -depth relationship (Figure 11). This is similar to the F_n -Quaternary thickness fit of Chapman et al. (2006). However, they used a constant V_{s1} for Quaternary strata in their analysis to fit a CPT dataset containing < 40 measurements, whereas I fit a power law function to over 2,700 measurements to show that F_n can be reasonably estimated independently of V_{s1} using Quaternary thickness alone.

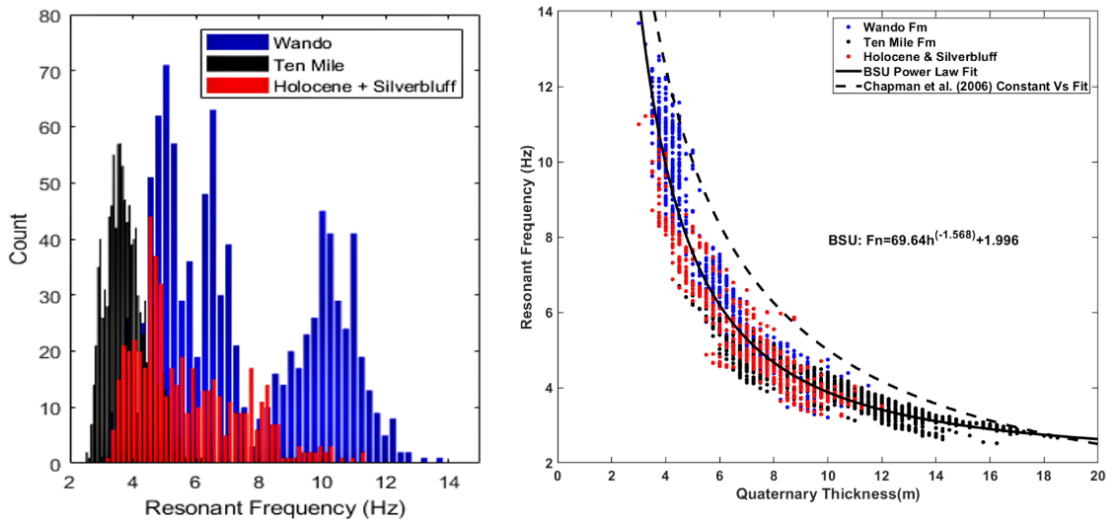


Figure 11. (a) F_n histogram by bulk lithology and (b) F_n - Quaternary thickness cross plot color coded by bulk lithology. A power law function fit to the BSU data is (solid black line) from equation 2 and constant velocity of 200 m/s - F_n relationship (dashed line) used by Chapman et al. (2006).

Constructing a Regional Site Response Parameter Database for the Greater Charleston Region

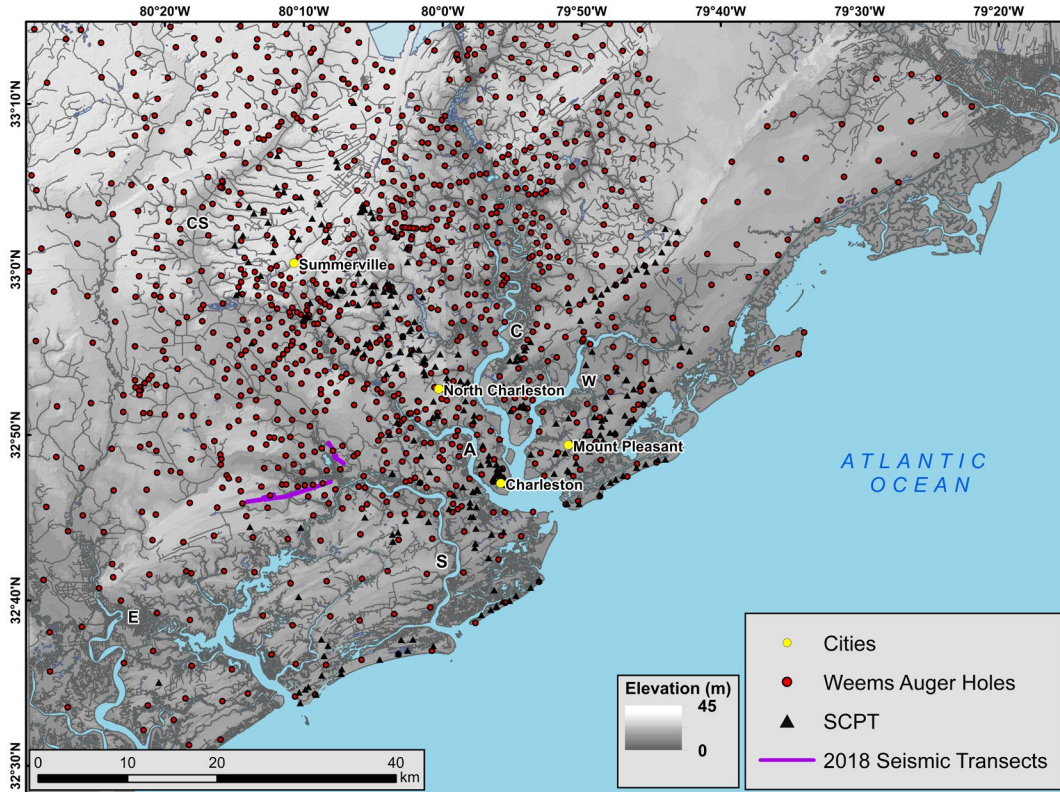


Figure 12. Greater Charleston region topographic map showing BSU seismic transects (purple lines), auger holes (Weems et al., 2014) (red circles), and SCPT sites from Gathro (2018) (black triangles). Major cities (yellow circles) and major rivers and waterways are labeled. A=Ashley River, C=Cooper River, W=Wando River, S=Stono River, E=Edisto River, CS=Cypress Swamp.

More than 300 SCPT measurements have been obtained for the greater Charleston region (Andrus et al., 2006; Gathro, 2018; Figure 12). Additionally, about 1000 shallow auger holes define Quaternary thickness across the region (Weems et al., 2014; Figure 12). Together, these datasets span a total area of ~5,000 square kilometers of the greater Charleston region. I integrate this large spatial database with my V_{s1} and results to regionally estimate F_n . I obtained the technical report of Gathro (2018) that summarized

the work of Andrus et al. (2006), Mohanan et al. (2006), and Heidari (2011), and contains 233 geometric mean, depth interval Vs values for 11 different members of prevalent Quaternary formations in the region. In increasing age this includes beach-barrier island sand and clayey sand and clay facies of Holocene deposits (Qhs), Silver Bluff Fm (Qsbs & Qsbc), Wando Fm (Qws, Qwc, & Qwls), Ten Mile Hill Beds Fm (Qts & Qtc), Ladson Fm (Qlc), and the Penholoway Fm (Qps & Qpc). Additionally, this technical report contains information for >300 individual SCPT sites containing position, lithologic, and Quaternary thickness information, but provide no Vs information.

To obtain the Vs averages for each stratigraphic unit and thickness, I compute a running average of the geometric mean from the >4,000 individual SCPT Vs measurements. I apply direct weighting to the running average data by duplicating each column a specific number of times based on the number of measurements the mean value signifies. This proved to be critical from an uncertainty standpoint when fitting individual stratigraphic units. Vs-depth equations were fit to each lithologies running average dataset, using both linear and polynomial models, where RMSE was compared. I found that each geologic unit was fit by a simple linear Vs-depth relationship (Figure 13). The average or bulk Quaternary Vs was calculated for each of the SCPT sites by applying

these lithology specific velocity-depth equations to corresponding SCPT sites (Figure 13).

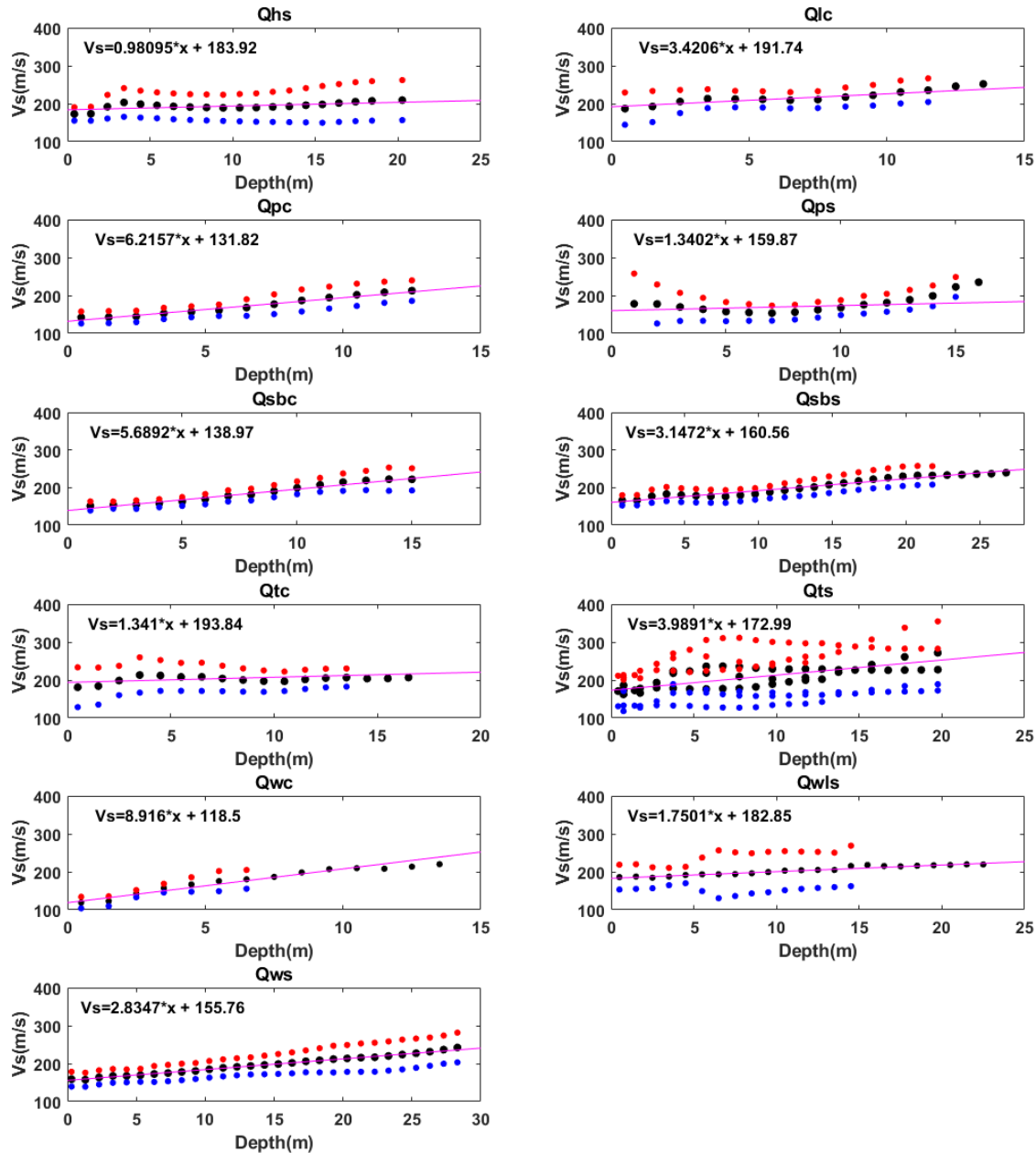


Figure 13. V_s (m/s)-depth (m) plots of weighted running average SCPT data (black), plus one standard deviation (red), and minus one standard deviation (blue) for 11 individual lithologies from Gathro (2018). The magenta line is the linear least squares fit to each running average dataset, and the equation for this line is shown in the top left corner of each plot.

Although the BSU dataset is useful for capturing lateral Vs, the SCPT data offers higher vertical resolution and spatial variability. For this reason, I use SCPT interpolations to estimate Vs for each auger hole location (Figure 14). I estimate Vs for the auger holes using a linear least-squares fit (equation 3: $V_{s1}=2.524h+167.4$) to the bulk weighted running average dataset, instead of using the lithology specific equations (Figure 14). The reasoning for this is that 1) the SCPT data consists of individual measurements in single lithologies, as indicated by nearby auger hole stratigraphic logs, 2) unlike the SCPT sites the majority of the auger holes contain numerous lithologies meaning the average Vs is related to a combined Vs-depth relationship for more than one unit, 3) because there appears to be no clear Vs-age relationship for the Quaternary units, and 4) neglecting the Ten Mile Hill Fm deposits, which show significant Vs gradient with increasing depth in both the BSU and Gathro (2018) datasets, the maximum difference between this bulk equation and the running average dataset is < 50 m/s. Obermeier (1996) suggested weakly acidic ground water has impeded bonding in the very quartz rich Quaternary deposits, possibly explaining why I do not measure a significant increase in Vs with formation age. In contrast to Vs increasing with age, as is commonly observed in low Vs sediments (e.g., Fumal et al., 1985), the 200-240 ka Ten Mile Hill Beds exhibit faster Vs than lithologically similar facies of the 730-970 ka Penholoway formation deposits.

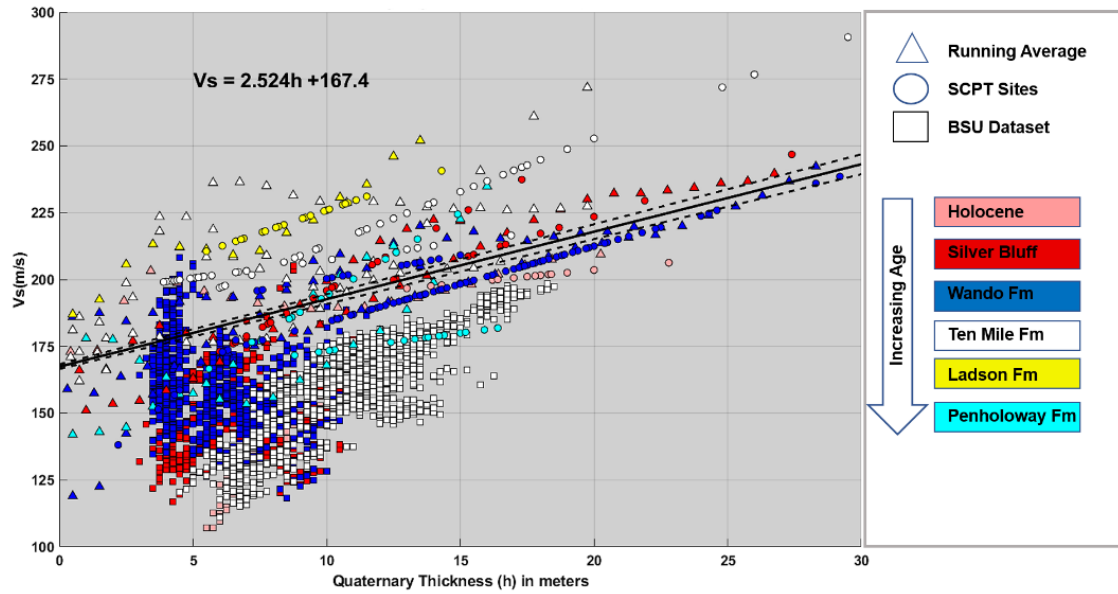


Figure 14. Vs-Quaternary thickness for all measurements from the greater Charleston region. The weighted running average of SCPT measurements from Gathro (2018) is indicated by triangles, individual SCPT sites are indicated by circles, and the 2-layer 2D grid search results are indicated by squares. Data points are colored by respective geologic formation. The solid black line indicates a linear least square fit (equation 3, shown in top left) to the weighted running average SCPT dataset used to estimate Vs as a function of Quaternary thickness for the auger holes.

Regionally, the mean Vs for all measurements is 168 m/s. Excluding the 2018 Boise State dataset yields a mean Vs of ~192 m/s. Based on Figures 14 and 15 I expect impedance to decrease with increasing Quaternary layer thickness, thus where Quaternary strata is anomalously thick, the average Vs approaches that of the underlying Tertiary strata. This reduces Fn and impedance. Where Quaternary strata is anomalously thin, I measure the highest Fn and impedance.

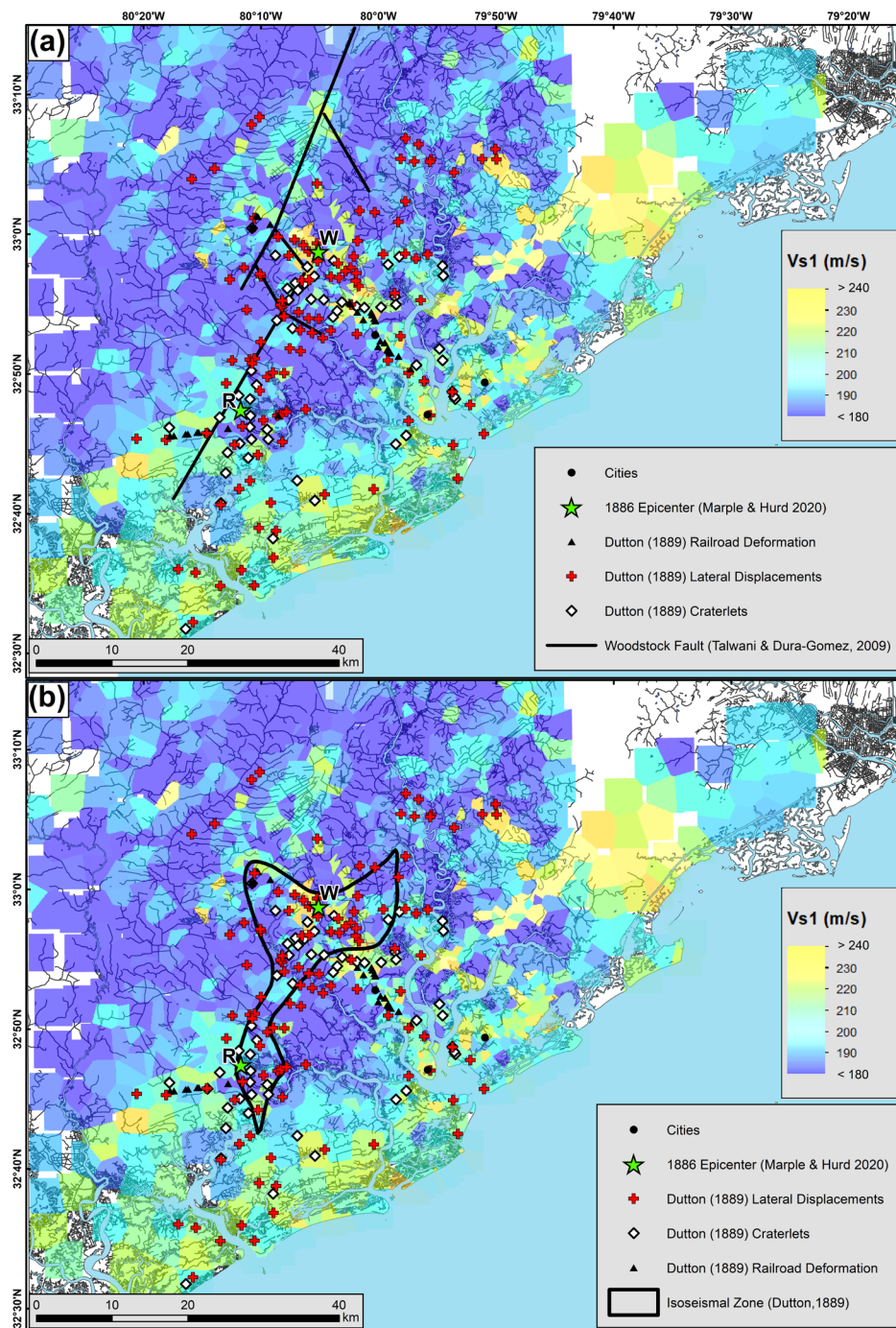


Figure 15. (a) Interpolated Quaternary V_s for the greater Charleston region derived from SCPT, BSU, and auger hole datasets. The Woodstock fault (Talwani and Dura-Gomez, 2009) is shown as a solid black line, the 1886 epicenter locations are indicated by green stars (Marple and Hurd, 2020). R=Rantowles and W=Woodstock. Deformation features mapped by Dutton (1889) include lateral displacements, liquefaction craterlets, and rail-line deformation. (b) Same map as above, but now the 1886 isoseismal map from Dutton (1889) is displayed.

To generate regional maps, I calculate F_n for all SCPT sites and auger hole locations using equation 1. Additionally, F_n was calculated for both datasets as a function of Quaternary thickness utilizing a power law fit (equation 4: $F_n=40.04h^{(-0.9174)}$) to the running average SCPT dataset (Figure 16). This was done solely for the purpose of comparison and assessment of the ability of the power law function to predict F_n based on Quaternary thickness alone. Because structural damage is less likely to occur at F_n values higher than 20Hz (< 2 m in Quaternary thickness) I removed data above this threshold while fitting the SCPT data with the power law function. The majority of my F_n observations are within 2 to 10 Hz, where significant structural damage is more likely to occur with respect to the range of building heights in the region. Thus, it is important that my accuracy while estimating resonant frequency below 20 Hz is not diminished by biasing the fitted equation by values above this threshold. Within the 2 to 20 Hz band, the mean difference between the approaches to estimate F_n for the SCPT sites is ~ 0.16 Hz, with a standard deviation of ~ 0.4 Hz. The mean difference between the approaches to estimate F_n for the auger holes within the same frequency range is ~ 0.03 Hz, with a standard deviation of ~ 0.1 Hz. This analysis illustrates that F_n can be accurately estimated using only Quaternary thickness.

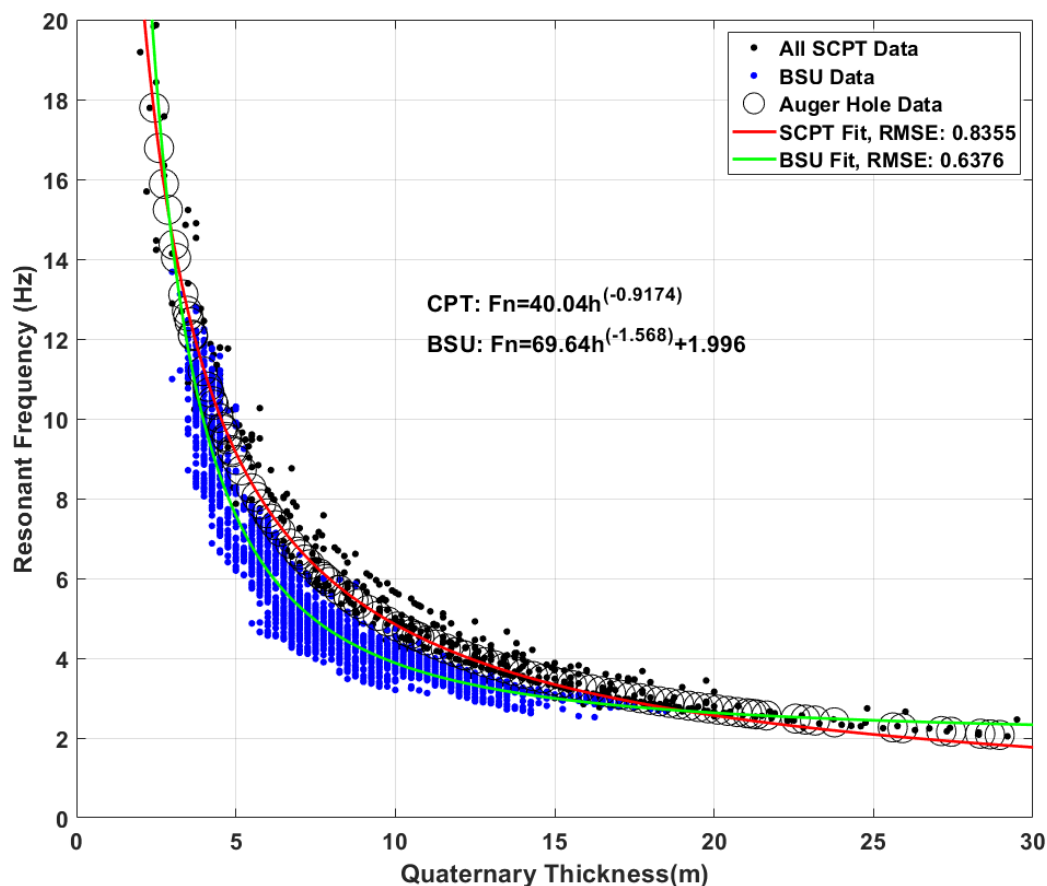


Figure 16. F_n -Quaternary thickness plot from SCPT data (black circles) BSU data (blue circles), and the larger circles are V_s derived from auger hole data. The green line shows the BSU power law fit (equation 2), while the red solid line shows the SCPT power law fit (equation 4).

Regional spatial sampling of the greater Charleston region is provided by the SCPT, BSU, and auger hole datasets. From these data the average F_n is ~ 6 Hz, and the average thickness of Quaternary deposits is about 8.5 m (Figures 16 and 17). In extreme cases I see ~ 1.5 Hz F_n values where Quaternary strata is upwards of 36 m thick and ~ 120 Hz where a thin veil of less than a half meter of Quaternary strata conceals Tertiary rock. However, the majority ($\sim 87\%$) of locations fall within the 2-10 Hz range meaning 1-4 story buildings are primarily at risk (Arnold, 2006). Less than 0.2% of observations fall

below 2 Hz, ~10.6% from 10-20 Hz, and 2% are above 20 Hz. Notably, 64% of the data fall within 2-8 Hz.

Spatial Variability in V_s , Quaternary Thickness, and F_n

I observe a trend of seaward thickening of Quaternary strata consistent with the regional geology described by Weems (2002). This drives F_n to lower frequencies. Along the north-south extent of the coastline, and extending inland ~8-9 km, I observe Quaternary thicknesses of 15-30 meters and Quaternary V_s of 190-220 m/s which corresponds to F_n values of 2-4 Hz. I observe that low F_n values extend inland adjacent to major bays, harbors, and major river inlets. Examples include the mouth of the Ashley, Cooper, and Wando Rivers that converge into Charleston Harbor. Similarly, I see the same pattern near the mouth of the Stono and Edisto Rivers, and other prominent inlets and bays further south along the coastline. Further upstream from these major tributaries, greater F_n variability is noted. I suggest that F_n increases where fluvial erosional processes prevail. The lowest Quaternary V_s is observed along these rivers, marshes, swamps, and estuaries where Holocene deposits are present (Figure 15). Two areas which don't follow the general trend of inland thinning of Quaternary sediments includes a northeast elongated region of F_n values in the 2-10 Hz range centered near the southern isoseismal region and a similarly oriented region spanning a length of ~25 km extending along the northern segment of the Woodstock fault near Summerville.

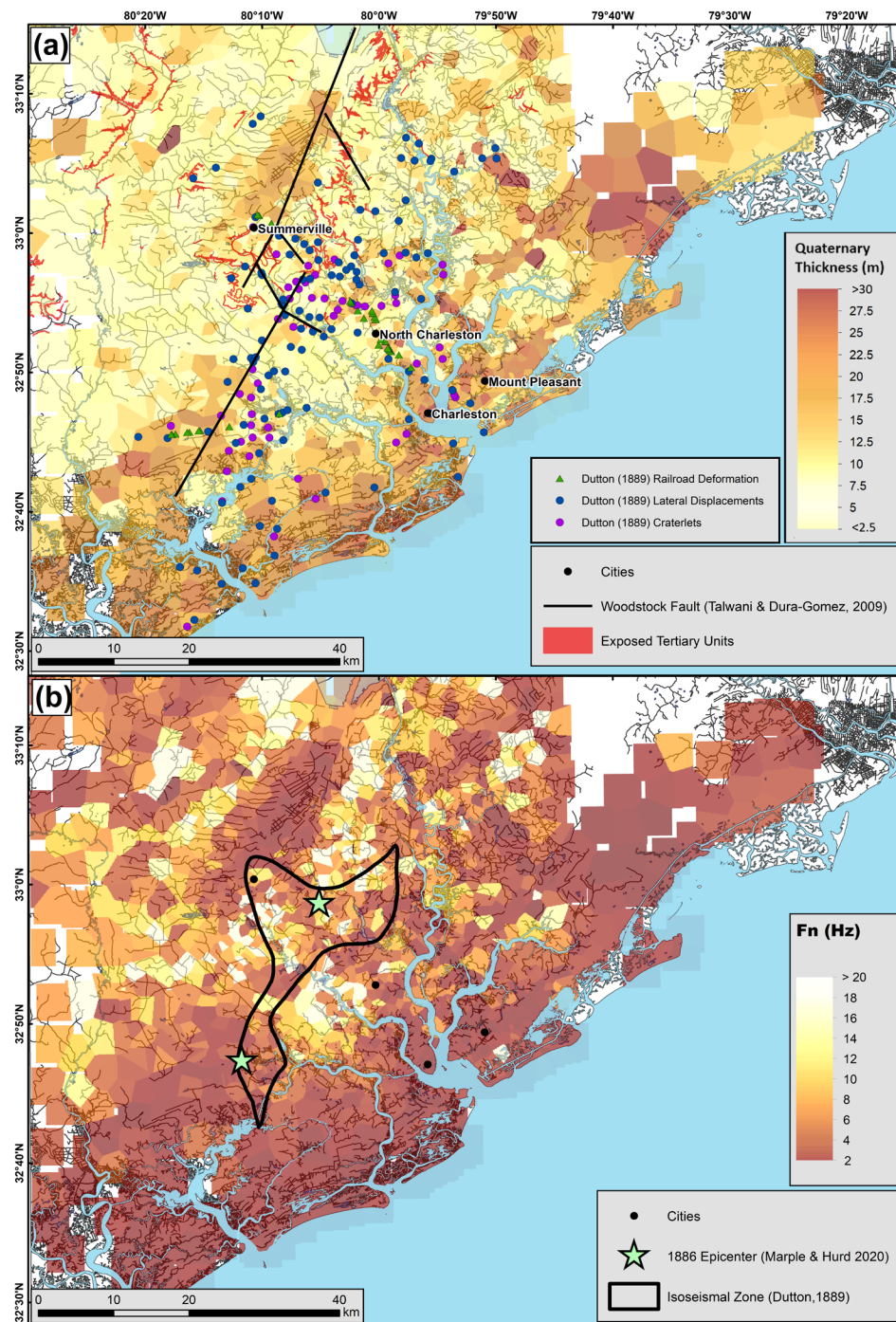


Figure 17. (a) Quaternary thickness map for the greater Charleston region. The Woodstock fault (Talwani and Dura-Gomez, 2009) is shown as a black line, deformation features mapped by Dutton (1889) include lateral displacements, liquefaction craterlets, and rail-line deformation. Exposed Tertiary rocks are indicated by red polygons. (b) Resonant frequency map for the greater Charleston region. The 1886 epicenter locations (green stars) from Marple & Hurd (2020) and the Dutton (1889) isoseismal zone (black polygon)

In the southern isoseismal zone I note relatively uniform Quaternary thicknesses corresponding to F_n values dominantly in the 2-8 Hz range (Figure 17). In this region near the presumed Rantowles epicenter, I observe Quaternary V_s typically slower than 180 m/s (Figure 15). This low velocity zone extends ~18 km to the northeast to the Ashley River. The low V_s zone then continues northwest along the inferred location of the Sawmill Branch left step along the Woodstock fault. Near the Sawmill Branch the low V_s zone is coincident with lateral spread and liquefaction craterlet features formed in 1886.

In the northern isoseismal zone and in the vicinity of the Woodstock epicenter, I observe high variability in Quaternary V_s , and in general much faster V_s (Figure 15). Similarly, I observe significant variability in F_n which ranges from 4-20 Hz (Figure 17). The higher variability in V_s in the northern isoseismal zone is attributed to a transition from late Pleistocene deposits to significantly older Middle-Early Pleistocene units such as the Ladson (240-730 ka) and Penholoway (730-970 ka) Formations to the west of the Woodstock fault. Additionally, Tertiary deposits are exposed to the east of the northern strand of the Woodstock fault in an area where rivers are deeply incised.

I note a pattern of northeastern trending deformation features within the southern isoseismal zone, generally following the length of the southern segment of the Woodstock fault. In the northern isoseismal zone the deformation features span a broad area centered below the Woodstock epicentral location. Curiously, very little deformation was identified to the west of Summerville and the proposed location of the northern segment of the Woodstock fault. Despite dominantly low V_s values west of the proposed Woodstock fault, no liquefaction features were mapped in this area. Given the close

proximity to the Woodstock fault, epicenter locations, and the presence of liquefaction along the coastline, sometimes greater than 20 km from the proposed epicenter locations, it is surprising that I do not see more liquefaction to the west. One possible explanation is that the ground water table was significantly lower in this region during the 1886 earthquake. This is not evident from water table depths recorded from the SCPT sites, or inferred from surface elevations. Another explanation is that the epicenter of 1886 event was farther to the south or east. A third explanation is that the dominant lithologies West of the northern strand of the Woodstock fault, which include some of the oldest Quaternary deposits in the region such as the Penholoway and Ladson Formations, are less susceptible to liquefaction. Obermeier (1996) suggested that deposits older than 250 ka, such as the Penholoway and Ladson formations, have very low susceptibility to liquefaction due to diagenetic changes leading to stiffer soil structure. However, these deposits should exhibit higher Vs if this is true. However, I propose that liquefaction was not identified in this region because it was less populated and more difficult to traverse in 1886, meaning there were less firsthand accounts of the effects of the earthquake, which reduced the need for investigation of surface deformation features.

Liquefaction and Ground Deformation Potential

I sample the regional Quaternary thickness, F_n , and V_{s1} grids (Figure 15 & 17) at the 1886 earthquake deformation locations mapped by Dutton (1889). While I do not identify distinct, individual patterns in the aforementioned parameters between the liquefaction craterlets, lateral displacements, and rail-line damage, I note patterns for all 201 deformation features. I observe 53% of deformation features occur in locations where Quaternary thickness is $<10\text{m}$, and 98% occur at locations where sediment

thickness is <20 m. About 60% of these deformation features occur where V_{s1} is <200 m/s, and 92% occur where V_{s1} is <220 m/s. A total of 83% of deformation features correspond to F_n values within the 2-10 Hz range. Notably < 6% of these features occur at locations with $F_n > 20$ Hz, which could be an artifact of less calibration points near these locations or locational uncertainty in the deformation features, but this still supports my approach to apply a 20 Hz cutoff based on anticipating less damage occurring at $F_n > 20$ Hz.

MASW and SCPT differences

Because the average V_s value derived from all BSU MASW data for Quaternary strata is about 30 m/s less than the average V_s value estimated from all SCPT data, I compare the two approaches. Differences may stem from data collection or processing approaches, or lithologic sampling differences.

SCPT data are a surface-to-downhole measurement technique. Here, a seismic receiver embedded in a cone tip is typically advanced at depth intervals of 0.5 or 1 m. A relatively high frequency seismic source is located at the surface. V_s is estimated at each receiver depth by measuring speed of sound travel time between source and receiver with a straight ray path assumption (Hunter et al., 2002). The straight ray assumption is valid under uniform velocity conditions, and errors may result from more complex arrival paths. This method provides strong coupling between the geophone and formation being measured, and V_s discrepancies between this method and suspension logging techniques is largely attributed to first arrival time picking and source frequency (Hunter et al., 2002). Gathro (2018) noted that errors in downhole V_s are typically greatest when the source-to-cone offset is largest, and when high contrasts in stiffness between soil layers

are present. In contrast, the MASW approach is obtained by relatively low frequency surface measurements that provide bulk property estimates averaged over the spatial range of the geophone array. Both vertical and horizontal resolution is much lower for MASW data, but MASW does not suffer from high frequency scattering effects. V_s estimates from both approaches assume uniform subsurface conditions at the point of measurement.

My MASW measurements were made only in the southern isoseismal region, an area where no SCPT measurements are located, meaning no in situ comparison and calibration can be conducted. In contrast, the SCPT measurements were made throughout greater Charleston region. As such, my MASW dataset contains measurements on several extremely low V_s Holocene deposits not sampled with SCPT. Furthermore, the SCPT data sample several compositionally similar, yet significantly older Quaternary units such as the Penholoway Formations, which is at least 490 Ka older than the Ten Mile Hill beds. Neither approach is sensitive to stratigraphic or depositional complexities such as grain size, clay content, sorting, or porosity, which can influence V_s .

V_s difference between MASW and SCPT methods is minor with respect to the full range of V_s for the Quaternary deposits and because the majority of the MASW data fall within +/- one sigma of the SCPT data. Xia et al. (2002) performed a direct comparison between MASW and down borehole suspension logger measurement approaches to estimate V_s . They noted that the differences between MASW and direct borehole measurements appeared to be random and generally agree more than 85% of the time. Hunter et al. (2002) observed even smaller relative differences between the two techniques, noting about a 9% difference. Here, I report an average difference of 18 %.

Assuming accurate depth estimates to the base of Quaternary strata, F_n estimates will differ by $\frac{1}{4}$ times the V_s difference. For my dataset averages, this suggests a F_n difference as high as ~ 2.3 Hz where Quaternary thickness is ~ 3 m, and a difference as low as ~ 0.1 Hz where Quaternary thickness is ~ 18 meters (Figure 16b). I suggest that this is an acceptable difference given that actual site resonances may be influenced by more than just the upper layer properties (e.g., interference effects). Thus, I conclude that my F_n estimates are reasonable for my study area. Beyond F_n and shallow V_s estimates, other key site response parameters are required in tandem to fully characterize the risk associated with earthquake hazards. These parameters include characterization of potential earthquake sources and magnitudes, distance from the source, the directionality of the energy released, site amplification, liquefaction probability, and attenuation parameters.

My results illustrate that fundamental resonant frequency, a critical site response parameter can be reasonably assessed over a broad region of the eastern seaboard where the thickness of the layers above a shallow high impedance boundary is known if the V_s for the overlying strata is well calibrated.

Fault Interpretations

I identify a 1 km wide fault bounded deformation zone on CSX, in a profile which otherwise shows mostly flat lying reflectors (Figure 18). I interpret this region as two steeply dipping faults which form a broad anticlinal fold. This fold lies within the southern isoseismal zone near surface deformation features identified by Dutton (1889). The eastern most of these two faults appears to be in line with the fault interpretation of Pratt et al. (2016) (Figure 18), where they proposed a new fault interpretation in this

region on the basis of GPR profiles and elongated river meander bends and river truncations. Additionally, I observe two near vertical faults on Hughes 1 (Figure 18) transect, the western most of which also aligns with fault interpretations from Pratt et al. (2016). The faults identified on Hughes 1 have the opposite dip polarity as the faults identified on the CSX profile, suggesting that these structures are not connected. Marple and Miller (2006) identified a ~5 km wide zone of faulting along the USC-5 seismic profile. I suggest that faulting observed further to the east on the Hughes 1 and CSX seismic profiles is evidence that the Woodstock fault comprises a laterally (east-west) extensive zone of deformation within my study area, as opposed to a single discrete feature such as was identified by Talwani & Dura-Gomez (2009).

I observe mostly flat-lying reflectors along the Martin Street profile, with offset and tilted reflectors within an 800 m wide zone (Figure 18). These faults are near the Talwani and Dura-Gomez (2009) proposed location of the southern segment of the Woodstock fault (Figure 14c). The faults share a similar dip polarity and angle to faulting observed on the eastern side of the USC-5 seismic profile (Figure 18) (Marple and Miller, 2006). The faults identified on Martin Street are either connected to those on the eastern side of USC-5 or individual structures within the ~5 km wide zone of faulting identified on the USC-5 transect. If these faults are connected, it would suggest a more northerly strike orientation of the southern strand of the Woodstock fault than was proposed by Talwani and Dura-Gomez (2009).

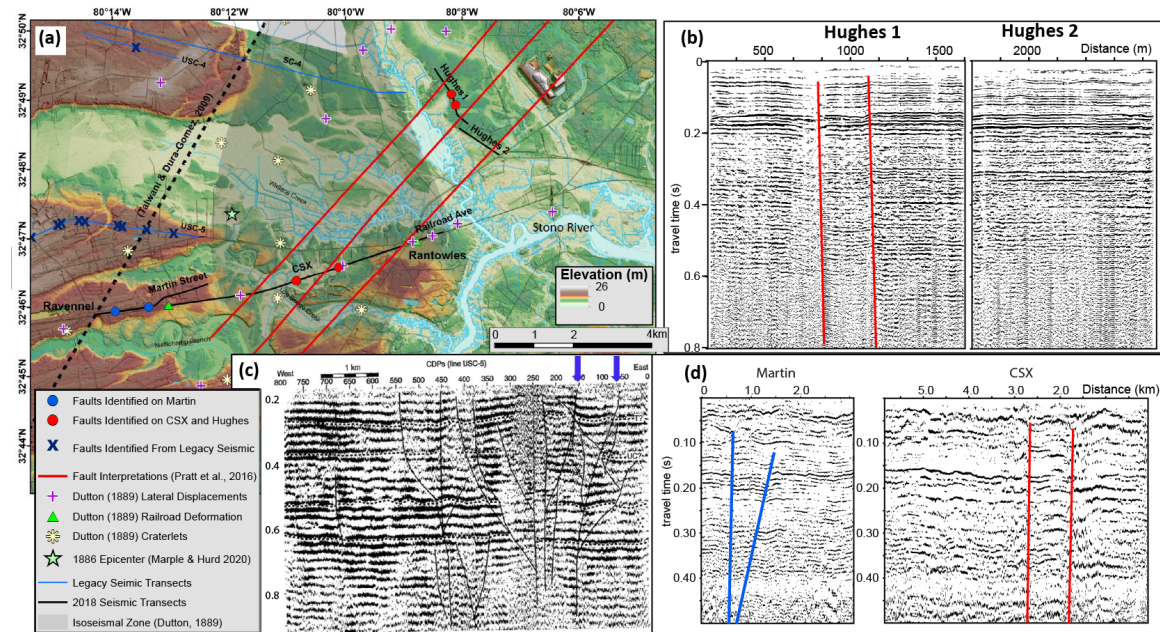


Figure 18. (a) Map of my study area showing deformation features, southern isoseismal zone (Dutton, 1889), BSU seismic profiles (black lines), and the Rantowles 1886 epicenter location (green star) from Marple and Miller. (2020). Faults on CSX and Hughes1 (red circles). Faults on Martin St (blue circles) as well as faults identified on USC-5 legacy seismic profile (blue Xs). The proposed location of the Woodstock Fault from Talwani and Dura-Gomez (2009) is indicated by the dashed black line, and proposed fault locations from Pratt et al. (2016) are indicated by the dashed red lines. (b) Reflection imagery from Hughes 1 and 2 in two-way travel time with 3:1 vertical exaggeration. Faults identified on Hughes 1 are shown in red. (c) USC-5 reflection imagery in two-way travel time from Marple and Miller (2006), the two blue arrows indicate faults that may be connected to the structures we observe on Martin St. (d) CSX (right) and Martin St (left) reflection imagery in two-way travel time with 6:1 vertical exaggeration. Fault interpretations are shown in red for CSX and in blue for Martin Street on (d).

CHAPTER FIVE: CONCLUSIONS

Earthquake site response estimates and fault kinematics are needed to fully assess earthquake hazards for the Charleston area. Fourteen kilometers of high-resolution seismic land streamer data provide site response controls through estimates of shallow V_s and the thickness of shallow soils that lie upon a high seismic impedance boundary. Although my focus was within the southern isoseismal region of the 1886 Charleston earthquake, I generated V_s and F_n maps for the greater metropolitan Charleston area by utilizing a regional database of complementary measurements. Overlapping measurements derived from borehole and SCPT data help validate my models. The spatial distribution of surface deformation features resulting from the 1886 earthquake correlate with low Quaternary V_s , high impedance, and low F_n regions. Faults that I identify lie within the 1886 deformation zone and are consistent with past structural interpretations. Identified faults that lie below low V_s zones may have moved in 1886 to produce shallow soil deformation features. My seismic land streamer approach to assessing earthquake hazards for the Charleston region is applicable to other regions within the Atlantic Coastal Plain with similar geologic and tectonic environments.

REFERENCES

- Ambraseys, N. N., & Menu, J. M. (1988). Earthquake-induced ground displacements. *Earthquake engineering & structural dynamics*, 16(7), 985-1006.
- Amick, D., & Gelinas, R. (1991). The search for evidence of large prehistoric earthquakes along the Atlantic seaboard. *Science*, 251(4994), 655-658.
- Andrus, R. D., Fairbanks, C. D., Zhang, J., Camp III, W. M., Casey, T. J., Cleary, T. J., & Wright, W. B. (2006). Shear-wave velocity and seismic response of near-surface sediments in Charleston, South Carolina. *Bulletin of the Seismological Society of America*, 96(5), 1897-1914.
- Arnold, C. (2006). Seismic issues in architectural design. *Designing for earthquakes. A manual for architects*. FEMA, 454, 1-54.
- Bakun, W. H., and Hopper, M. G. (2004). Magnitudes and locations of the 1811–1812 New Madrid Missouri and the 1886 Charleston, South Carolina, earthquake, *Bulletin of the Seismological Society of America*. 94, 64–75.
- Bollinger, G. A., (1977). Reinterpretation of the intensity data for the 1886 Charleston, South Carolina, earthquake, in Rankin, D.W., ed., *Studies Related to the Charleston, South Carolina Earthquake of 1886: A Preliminary Report*, U.S. Geological Survey Professional Paper 1028-B, p. 17-32.
- Boore, D. M., & Atkinson, G. M. (2008). Ground-motion prediction equations for the average horizontal component of PGA, PGV, and 5%-damped PSA at spectral periods between 0.01 s and 10.0 s. *Earthquake Spectra*, 24(1), 99-138.
- Boore, D. M. (2016). Determining generic velocity and density models for crustal amplification calculations, with an update of the generic site amplification for. *Bulletin of the Seismological Society of America*, 106(1), 313-317.

- Buckner, J. C. (2011). Crustal Structure in a Mesozoic Extensional Terrane: The South Georgia Rift and the Epicentral Area of the 1886 Charleston, South Carolina, Earthquake (Doctoral dissertation, Virginia Tech).
- Chapman, M. C., Martin, J. R., Olgun, C. G., & Beale, J. N. (2006). Site-response models for Charleston, South Carolina, and vicinity developed from shallow geotechnical investigations. *Bulletin of the Seismological Society of America*, 96(2), 467-489.
- Chapman, M. C., & Beale, J. N. (2008). Mesozoic and Cenozoic faulting imaged at the epicenter of the 1886 Charleston, South Carolina, earthquake. *Bulletin of the Seismological Society of America*, 98(5), 2533-2542.
- Chapman, M. C., & Beale, J. N. (2010). On the geologic structure at the epicenter of the 1886 Charleston, South Carolina, earthquake. *Bulletin of the Seismological Society of America*, 100(3), 1010-1030.
- Chapman, M. C., Beale, J. N., Hardy, A. C., and Wu, Q. (2016). Modern Seismicity and the Fault Responsible for the 1886 Charleston, South Carolina, Earthquake. *Bulletin of the Seismological Society of America*, 106(2), 364-372.
- Council, B. S. S. (2009). NEHRP recommended seismic provisions for new buildings and other structures. Rep. FEMA P, 750.
- Cramer, C. H., & Boyd, O. S. (2014). Why the New Madrid earthquakes are M 7–8 and the Charleston earthquake is ~ M 7. *Bulletin of the Seismological Society of America*, 104(6), 2884-2903.
- Dutton, C. E. (1889). The Charleston earthquake of August 31, 1886, in Ninth Annual Report of the U.S. Geological Survey to the Secretary of the Interior, J.W. Powell, Director, U.S. Geological Survey, Department of the Interior, U.S. Government Printing Office, Washington, D.C., 203–528.
- Frankel, A. D., Petersen, M. D., Mueller, C. S., Haller, K. M., Wheeler, R. L., Leyendecker, E. V., Wesson, R. L., Harmsen, S. C., Cramer, C. H., Perkins, D. M., Rukstales, K. S. (2002). Documentation for the 2002 update of the national seismic hazard maps. US Geological Survey Open-File Report, 420, 39.

- Fumal, T., Tinsley, J. C., & Ziony, J. E. (1985). Mapping shear-wave velocities of near-surface geologic materials. *Evaluating Earthquake Hazards in the Los Angeles Region-An Earth-Science Perspective*. US Geological Survey Professional Paper, 1360, 101-126.
- Gathro, J. D. (2018). *Liquefaction Probability Analysis of Quaternary Deposits in the Greater Charleston, South Carolina Area* (Doctoral dissertation, Clemson University).
- Gao, L., Xia, J., Pan, Y., & Xu, Y. (2016). Reason and condition for mode kissing in MASW method. *Pure and Applied Geophysics*, 173(5), 1627-1638.
- Heidari, T. (2011). "Characterizing liquefaction potential of Pleistocene soil deposits in the Charleston area, South Carolina." Ph.D. Dissertation, Clemson University, Clemson, SC.
- Heidari, T., & Andrus, R. D. (2012). Liquefaction potential assessment of Pleistocene beach sands near Charleston, South Carolina. *Journal of geotechnical and geoenvironmental engineering*, 138(10), 1196-1208.
- Hunter, J. A., Pullan, S. E., Burns, R. A., Gagne, R. M., & Good, R. L. (1984). Shallow seismic reflection mapping of the overburden-bedrock interface with the engineering seismograph—Some simple techniques. *Geophysics*, 49(8), 1381-1385.
- Hunter, J. A., Benjumea, B., Harris, J. B., Miller, R. D., Pullan, S. E., Burns, R. A., & Good, R. L. (2002). Surface and downhole shear wave seismic methods for thick soil site investigations. *Soil Dynamics and Earthquake Engineering*, 22(9-12), 931-941.
- Liberty, L. M., St. Clair, J., Mikesell, T. D., & Schermerhorn, W. D. (2021). Resonant Frequency Derived from the Rayleigh-Wave Dispersion Image: The High-Impedance Boundary Problem. *Bulletin of the Seismological Society of America*, 111(1), 77-86.

- Marple, R. T., & Talwani, P. (1993). Evidence of possible tectonic upwarping along the South Carolina coastal plain from an examination of river morphology and elevation data. *Geology*, 21(7), 651-654.
- Marple, R., & Miller, R. (2006). Association of the 1886 Charleston, South Carolina, earthquake and seismicity near Summerville with a 12° bend in the East Coast fault system and triple-fault junctions. *Southeastern Geology*, 44(3), 101-127.
- Marple, R. (2011). Comment on the Companion Articles “Finding Faults in the Charleston Area, South Carolina: 1. Seismological Data” by I. Durá-Gómez and P. Talwani and “Finding Faults in the Charleston Area, South Carolina: 2. Complementary Data” by P. Talwani and I. Durá-Gómez. *Seismological Research Letters*, 82(4), 599-605.
- Marple, R. T., & Hurd, J. D. (2020). Interpretation of lineaments and faults near Summerville, South Carolina, USA, using LiDAR data: implications for the cause of the 1886 Charleston, South Carolina, earthquake. *Atlantic Geology: Journal of the Atlantic Geoscience Society/Atlantic Geology: revue de la Société Géoscientifique de l'Atlantique*, 56, 73-95.
- Mavko, G., Mukerji, T., & Dvorkin, J. (2009). *The Rock Physics Handbook: Tools for Seismic Analysis of Porous Media* (2nd ed.). Cambridge: Cambridge University Press. doi:10.1017/CBO9780511626753
- Michaels P., 2018. Basic seismic utilities software, Available at: https://scholarworks.boisestate.edu/geo_data/3, Accessed 2019/01/10.
- Michaels, P., and R. B. Smith (1997). Surface wave inversion by neural networks (radial basis functions) for engineering applications, *J. Environ. Eng. Geophys.* 2, no. 1, 65–76.
- Mikesell, T. D., Gribler, G., Xu, Z., & Haney, M. M. (2017). High-resolution dispersion images from deblurred MASW. In *SEG Technical Program Expanded Abstracts 2017* (pp. 5284-5288). Society of Exploration Geophysicists.
- Mohan, N. P., Fairbanks, C. D., Andrus, R. D., Camp, W. M., Clearly, T. J., Casey, T. J., and Wright, W. B. (2006). “Electronic files of shear wave velocity and cone

- penetration test measurements from the Greater Charleston area, South Carolina.” Data Report to the U.S. Geological Survey, Award No. 05HQGR0037, Civil Engineering Department, Clemson University, Clemson, SC.
- Obermeier, S. F. (1996). Use of liquefaction-induced features for paleoseismic analysis—an overview of how seismic liquefaction features can be distinguished from other features and how their regional distribution and properties of source sediment can be used to infer the location and strength of Holocene paleo-earthquakes. *Engineering Geology*, 44(1-4), 1-76.
- Odum, J. K., Williams, R. A., Stephenson, W. J., & Worley, D. M. (2003). Near-surface S-wave and P-wave seismic velocities of primary geological formations on the Piedmont and Atlantic Coastal Plain of South Carolina, USA (No. 2003-43).
- Park, C.B., Miller, R.D., and Xia, J., 1999, Multichannel analysis of surface waves, *Geophysics*, 64, 800–808.
- Petersen, M.D., Moschetti, M.P., Powers, P.M., Mueller, C.S., Haller, K.M., Frankel, A.D., Zeng, Yuehua, Rezaeian, Sanaz, Harmsen, S.C., Boyd, O.S., Field, Ned, Chen, Rui, Rukstales, K.S., Luco, Nico, Wheeler, R.L., Williams, R.A., and Olsen, A.H., 2014, Documentation for the 2014 update of the United States national seismic hazard maps: U.S. Geological Survey Open-File Report 2014–1091, 243 p., <http://dx.doi.org/10.3333/ofr20141091>.
- Pratt, T.L., Shah, A.K., Horton, J.W., Chapman, M.C., and Beale, J.N., 2016, Recent fault activity in the 1886 Charleston, South Carolina earthquake epicentral area and its relation to buried structures, *Seismological Research Letters*, v. 87, p. 486-487.
- SeisSpace-ProMAX, 2017: SeisSpace-ProMAX. Halliburton.
<https://www.landmark.solutions/SeisSpace-ProMAX>
- Shearer, P. M., & Orcutt, J. A. (1987). Surface and near-surface effects on seismic waves—theory and borehole seismometer results. *Bulletin of the Seismological Society of America*, 77(4), 1168-1196.

- Talwani, P., and Durá-Gómez, I. (2009). Finding faults in the Charleston area, South Carolina: 2. Complementary data. *Seismological Research Letters*, 80(5), 901-919.
- Weems, R.E., Lemon, E.M., Jr., Gohn, G.S., and Houser, B.B. (1987). Detailed sections from auger holes and outcrops in the Clubhouse Crossroads, Johns Island, Osborn, and Ravenel quadrangles, South Carolina: U.S. Geological Survey Open-File Report 87-661, 159 p. (available online at <http://pubs.er.usgs.gov/publication/ofr87661>.)
- Weems, R. E., & Lewis, W. C. (2002). Structural and tectonic setting of the Charleston, South Carolina, region: Evidence from the Tertiary stratigraphic record. *Geological Society of America Bulletin*, 114(1), 24-42.
- Weems, R. E., Lewis, W. C., & Lemon Jr, E. M. (2014). Surficial geologic map of the Charleston region, Berkeley, Charleston, Colleton, Dorchester, and Georgetown Counties, South Carolina (No. 2013-1030). US Geological Survey.
- Wong, I., and 9 others, 2005, Potential losses in a repeat of the 1886 Charleston, South Carolina, Earthquake, *Earthquake Spectra*, v. 21, no 4, p. 1157-1184.
- Xia, J., Miller, R. D., & Park, C. B. (1999). Estimation of near-surface shear-wave velocity by inversion of Rayleigh waves. *Geophysics*, 64(3), 691-700.
- Xia, J., Miller, R. D., Park, C. B., Hunter, J. A., Harris, J. B., & Ivanov, J. (2002). Comparing shear-wave velocity profiles inverted from multichannel surface wave with borehole measurements. *Soil dynamics and earthquake engineering*, 22(3), 181-190.
- Xia, J., Xu, Y., Chen, C., Kaufmann, R. D., & Luo, Y. (2006). Simple equations guide high-frequency surface-wave investigation techniques. *Soil Dynamics and Earthquake Engineering*, 26(5), 395-403
- U.S. Geological Survey (2020). Comprehensive earthquake catalog, available at <https://earthquake.usgs.gov/earthquakes/search/> (last accessed April 2021).